

A new experimental approach for the exploration of topological quantum phenomena

M. Zahid Hasan,^{1,2,3} David Hsieh,^{1,4} Yuqi Xia,¹ L. Andrew Wray,¹ Su-Yang Xu,¹ and Charles L. Kane⁵

¹*Joseph Henry Laboratories, Department of Physics,
Princeton University, Princeton, NJ 08544, USA*

²*Princeton Institute for the Science and Technology of Materials,
School of Engineering and Applied Science, Princeton University, Princeton NJ 08544, USA*

³*Advanced Light Source, Lawrence Berkeley National Laboratory, Berkeley, California 94305, USA*

⁴*Department of Physics, Massachusetts Institute of Technology, Cambridge, MA 02139, USA*

⁵*Department of Physics and Astronomy, University of Pennsylvania, Philadelphia, PA 19104, USA*

The three-dimensional topological insulator (originally called "topological insulators") is the first example in nature of a topologically ordered electronic phase existing in three dimensions that cannot be reduced to multiple copies of quantum-Hall-like states. **Their topological order can be realized at room temperatures without magnetic fields and they can be turned into magnets and exotic superconductors leading to world-wide interest and activity in topological insulators.** These experimentally demonstrated unique properties of 3D topological insulators have turned the topic into a field of intense experimental activity. It is also only the third topologically ordered phase in weakly interacting systems to be discovered in nature, with the first two belonging to the quantum Hall-like topological insulator class consisting of the 2D integer quantum Hall state (IQH) and the 2D quantum spin Hall state (QSH). The 2D quantum spin Hall state (QSH) can be thought of as two copies of IQH put together leading to a time-reversal invariant version of IQH state. All of the 2D topological insulator examples (IQH, QSH) including the fractional one (FQH) involving Coulomb interaction are understood in the standard picture of quantized electron orbits in a spin-independent or spin-dependent magnetic field, **the 3D topological insulator defies such description and is a novel type of topological order which cannot be reduced to multiple copies of quantum-Hall-like states.** In fact, the 3D topological insulator exists not only in zero magnetic field, and differs from the 2D variety in three very important aspects: **1)** they possess topologically protected 2D metallic surfaces (a new type of 2DEG) rather than the 1D edges, **2)** they can work at room temperature (300K and beyond, large-gap topological insulators) rather than cryogenic (mK) temperatures required for the QSH effects and **3)** they occur in standard bulk semiconductors rather than at buried interfaces of ultraclean semiconductor heterostructures thus tolerate stronger disorder than the IQH-like states. One of the major challenges in going from quantum Hall-like 2D states to 3D topological insulators is to **develop new experimental approaches/methods to precisely probe this novel form of topological-order** since the standard tools and settings that work for IQH-state also work for QSH states. The method to probe 2D topological-order is exclusively with charge transport (pioneered by Von Klitzing in the 1980s), which either measures quantized transverse conductance plateaus in IQH systems or longitudinal conductance in quantum spin Hall (QSH) systems. In a 3D topological insulator, the boundary itself supports a two dimensional electron gas (2DEG) and transport is not (Z_2) topologically quantized hence *cannot* directly probe the topological invariants ν_o or the topological quantum numbers analogous to the Chern numbers of the IQH systems. This is *unrelated* to the fact that the present materials have some extrinsic or residual/impurity conductivity in their naturally grown bulk. In this paper, we review the birth of momentum- and spin-resolved spectroscopy as a new experimental approach and as a directly boundary sensitive method to study and prove topological-order in three-dimensions via the direct measurements of the topological invariants ν_o that are associated with the Z_2 topology of the spin-orbit band structure and opposite parity band inversions, which led to the experimental discovery of the first 3D topological insulator in Bi-Sb semiconductors (KITP Proceeding **2007** <http://online.itp.ucsb.edu/online/motterials07/hasan/> (2007), Nature 452, 970 (2008), Submitted **2007**) which further led to the discovery of the Bi_2Se_3 class - the most widely researched topological insulator to this date. We discuss the fundamental properties of the novel topologically spin-momentum locked half Dirac metal on the surfaces of the 3D topological insulators and how they emerge from topological phase transitions due to increasing spin-orbit coupling in the bulk. These electronic and spin properties of **topological surface states** discovered via the methods reviewed here are already guiding the interpretation of surface transport measurements as they are beginning to be possible further advancing the field potentially towards device applications. These methods and their derivatives are also being applied by many others world-wide for further investigations of topological-order and for discovering new topological insulator states as well as exotic topological quantum phenomena (the list is too long to review here). We also review how spectroscopic methods are leading to the identification of spin-orbit superconductors that may work as Majorana platforms and can be used to identify topological superconductors - yet another class of new state of matter.

I. The birth of momentum-resolved spectroscopy as a direct experimental probe of Topological-Order	2
II. Separation of insulating bulk from metallic surface states using incident photon energy modulated ARPES	4
III. Winding number count: Counting of surface Fermi surfaces enclosing Kramers points to identify topologically non-trivial surface spin-textured states	6
IV. Spin-resolving the surface states to identify the non-trivial topological phase and establish a 2D helical metal protected from backscattering	9
V. Identifying the origin of 3D topological order via a bulk band gap inversion transition	11
VI. Topological protection and tunability of the surface states of a 3D topological insulator	15
VII. Future directions: Identifying Majorana Platforms and Topological Superconductors	17
VIII. Supplementary materials	18
A. Growth method for high-quality single crystals	18
B. Resistivity characterization	19
C. ARPES	20
D. Systematic methods for separating bulk from surface electronic states	20
E. Confirming the bulk nature of electronic bands by comparison with theoretical calculations	22
F. Spin-orbit coupling is responsible for the unique Dirac-like dispersion behaviour of the bulk bands near E_F	22
G. Matching the surface state Fermi crossings and the topology of the surface Fermi surface in bulk insulating $\text{Bi}_{0.9}\text{Sb}_{0.1}$	24
H. Two-step fitting analysis procedure of Spin-Resolved ARPES measurements of insulating $\text{Bi}_{1-x}\text{Sb}_x$	25
I. Method of using incident photon energy modulated ARPES to separate the bulk from surface electronic states of Sb	25
J. Method of counting spin Fermi surface \vec{k}_T enclosures in pure Sb	27
K. Physical interpretation of n_M : the mirror Chern number and an analogy with the spin-Chern number	27

THE BIRTH OF MOMENTUM-RESOLVED SPECTROSCOPY AS A DIRECT EXPERIMENTAL PROBE OF TOPOLOGICAL-ORDER

Ordered phases of matter such as a superfluid or a ferromagnet are usually associated with the breaking of a symmetry and are characterized by a local order parameter [1]. The typical experimental probes of these systems are sensitive to order parameters. In the 1980s, two new phases of matter were realized by subjecting 2D electron gases at buried interfaces of semiconductor heterostructures to large magnetic fields. These new phases of matter, the 2D integer and 2D fractional quantum Hall states, exhibited a new and rare type of order that is derived from an organized collective quantum entangled motion of electrons [2–5]. These so-called “2D topologically ordered insulators” do not exhibit any symmetry breaking and are characterized by a topological number [6] as opposed to a local order parameter. The most striking manifestation of this 2D topological order is the existence of one-way propagating 1D metallic states confined to their edges, which lead to remarkable quantized charge transport phenomena. To date the experimental probe of their topological quantum numbers is based on charge transport, where measurements of the quantization of transverse magneto-conductivity $\sigma_{xy} = ne^2/h$ (where e is the electric charge and h is Planck’s constant) reveals the value of the topological number n that characterizes these quantum Hall states [7].

Recently, a third type of 2D topological insulator, the spin quantum Hall insulator, was theoretically predicted [8, 9] and then experimentally discovered [13]. This class of quantum Hall-like topological phases can exist in spin-orbit materials without external magnetic fields, and can be described as an ordinary quantum Hall state in a spin-dependent magnetic field. Their topological order gives rise to counter-propagating 1D edge states that carry opposite spin polarization, often described as a superposition of a spin up and spin down quantum Hall edge state (Figure 1). Like conventional quantum Hall systems, the 2D spin quantum Hall insulator (QSH) is realized at a buried solid interface. The first, and to date only, realization of this phase was made in $(\text{Hg,Cd})\text{Te}$ quantum wells using *charge transport* by measuring a longitudinal conductance of about $2e^2/h$ at mK temperatures [13]. The quantum spin Hall state (QSH) can be thought of as two copies of integer quantum Hall states (IQH) and protected by a \mathbb{Z}_2 invariant.

It was also realized that a fundamentally new type of genuinely three-dimensional topological order might be realized in bulk crystals without need for an external magnetic field [10–12]. Such a 3D topological insulator cannot be reduced to multiple copies of the IQH and such phases would be only the fourth type of topologically

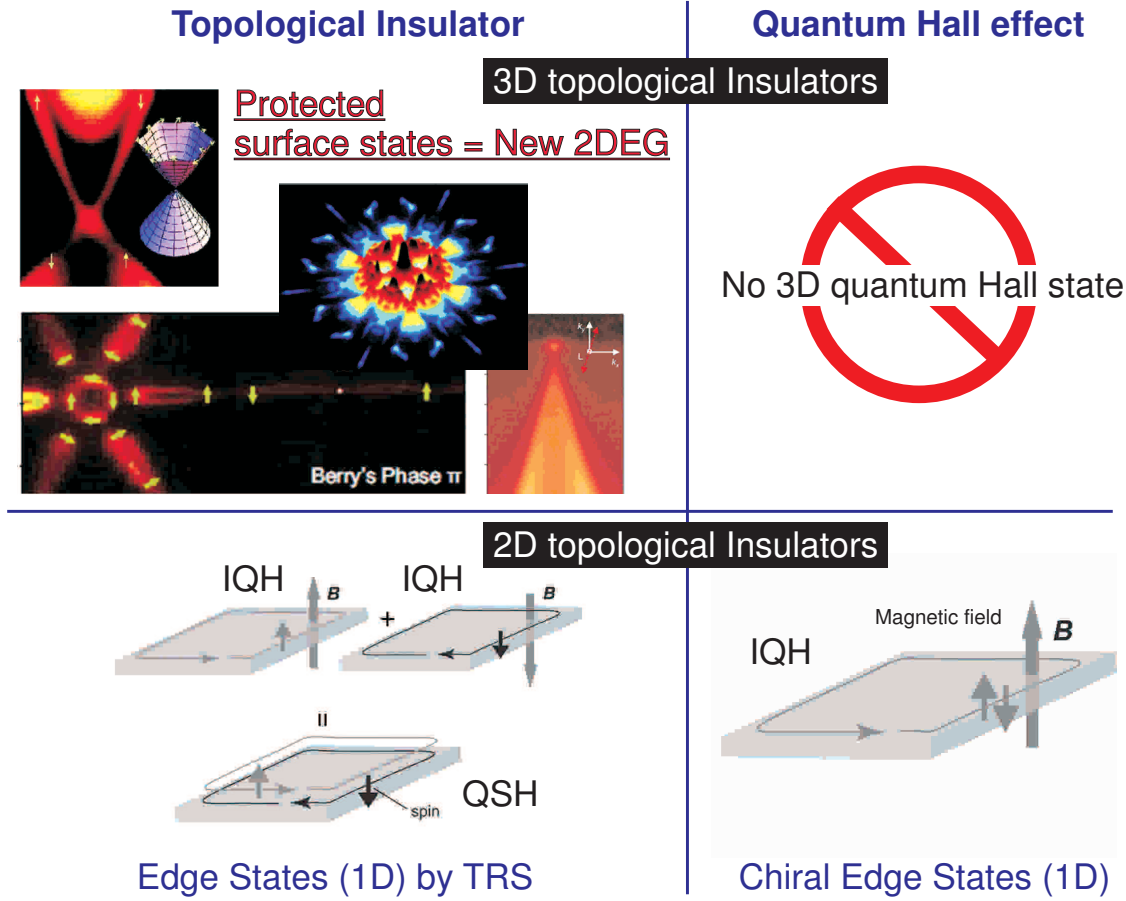


FIG. 1: **2D and 3D topological insulators in nature.** The 2D topological insulator class consists of the 2D quantum Hall states (IQH) and 2D quantum spin Hall state (QSH). The latter is constructed from two copies of the former. On the other hand, a 3D quantum Hall state is forbidden in nature, so the 3D topological insulator represents a new type of topologically ordered phase. The protected surface states form a novel type of topological metal (half Dirac metal) where electron's spin is locked to its momentum but exhibit no spin quantum Hall effect.

ordered phase to be discovered in nature, and the first type to fall outside the quantum Hall-like 2D topological states (IQH, FQH, QSH). Instead of having quantum-Hall type 1D edge state, these so-called 3D topological insulators would possess unconventional metallic 2D topological surface states called spin-textured helical metals, a type of 2D electron gas long thought to be impossible to realize. However, it was recognized that 3D topological insulators would NOT necessarily exhibit a topologically (Z2) quantized charge transport by themselves as carried out in a conventional transport settings of all quantum-Hall-like measurements. Therefore, their 3D topological quantum numbers (Z2), the analogues of n (Chern numbers), could not be measured via the charge transport based methods even if a complete isolation of surface charge transport becomes routinely possible. Owing to the 2D nature of the two surface conduction channels that contribute together in a 3D topological insulator case, it was theoretically recognized that it would not be possible to measure the topological invariants due to the lack of a quantized transport response of the 2D surface that

measures the Z2 topological invariants [12].

Here we review the development of spin- and angle-resolved photoemission spectroscopy (spin-ARPES) as the new approach/method to probe 3D topological order [14, 16], which today constitutes the experimental standard for identifying topological order in bulk solids also used by many others world-wide. We will review the procedures for i) separating intrinsic bulk bands from surface electronic structures using incident energy modulated ARPES, ii) mapping the surface electronic structure across the Kramers momenta to establish the topologically non-trivial nature of the surface states, iii) using spin-ARPES to map the spin texture of the surface states to reveal topological quantum numbers and Berry's phases and iv) measuring the topological parent compounds to establish the microscopic origins of 3D topological order. These will be discussed in the context of $\text{Bi}_{1-x}\text{Sb}_x$, which was the first 3D topological insulator to be experimentally discovered in nature and a textbook example of how this method is applied. The confluence of three factors, having a detailed spectroscopic procedure

to measure 3D topological order, their discovery in fairly simple bulk semiconductors and being able to work at room temperatures, has led to worldwide efforts to study 3D topological physics and led to over 100 compounds being identified as 3D topological insulators to date.

SEPARATION OF INSULATING BULK FROM METALLIC SURFACE STATES USING INCIDENT PHOTON ENERGY MODULATED ARPES

Three-dimensional topological order is predicted to occur in semiconductors with an inverted band gap, therefore 3D topological insulators are often searched for in systems where a band gap inversion is known to take place as a function of some control parameter. The experimental signature of being in the vicinity of a bulk band inversion is that the bulk band dispersion should be described by the massive Dirac equation rather than Schrodinger equation, since the system must be described by the massless Dirac equation exactly at the bulk band inversion point.

The early theoretical treatments [10, 23] focused on the strongly spin-orbit coupled, band-inverted $\text{Bi}_{1-x}\text{Sb}_x$ series as a possible realization of 3D topological order for the following reason. Bismuth is a semimetal with strong spin-orbit interactions. Its band structure is believed to feature an indirect negative gap between the valence band maximum at the T point of the bulk Brillouin zone (BZ) and the conduction band minima at three equivalent L points [24, 25] (here we generally refer to these as a single point, L). The valence and conduction bands at L are derived from antisymmetric (L_a) and symmetric (L_s) p -type orbitals, respectively, and the effective low-energy Hamiltonian at this point is described by the (3+1)-dimensional relativistic Dirac equation [26–28]. The resulting dispersion relation,

$E(\vec{k}) = \pm\sqrt{(\vec{v} \cdot \vec{k})^2 + \Delta^2} \approx \vec{v} \cdot \vec{k}$, is highly linear owing to the combination of an unusually large band velocity \vec{v} and a small gap Δ (such that $|\Delta/|\vec{v}|| \approx 5 \times 10^{-3} \text{Å}^{-1}$) and has been used to explain various peculiar properties of bismuth [26–28]. Substituting bismuth with antimony is believed to change the critical energies of the band structure as follows (see Fig.2). At an Sb concentration of $x \approx 4\%$, the gap Δ between L_a and L_s closes and a massless three-dimensional (3D) Dirac point is realized. As x is further increased this gap re-opens with inverted symmetry ordering, which leads to a change in sign of Δ at each of the three equivalent L points in the BZ. For concentrations greater than $x \approx 7\%$ there is no overlap between the valence band at T and the conduction band at L, and the material becomes an inverted-band insulator. Once the band at T drops below the valence band at L, at $x \approx 8\%$, the system evolves into a direct-gap insulator whose low energy physics is dominated by the spin-orbit coupled Dirac particles at L [10, 24].

High-momentum-resolution angle-resolved photoemis-

sion spectroscopy performed with varying incident photon energy (IPEM-ARPES) allows for measurement of electronic band dispersion along various momentum space (\vec{k} -space) trajectories in the 3D bulk BZ. ARPES spectra taken along two orthogonal cuts through the L point of the bulk BZ of $\text{Bi}_{0.9}\text{Sb}_{0.1}$ are shown in Figs 1a and c. A Λ -shaped dispersion whose tip lies less than 50 meV below the Fermi energy (E_F) can be seen along both directions. Additional features originating from surface states that do not disperse with incident photon energy are also seen. Owing to the finite intensity between the bulk and surface states, the exact binding energy (E_B) where the tip of the Λ -shaped band dispersion lies is unresolved. The linearity of the bulk Λ -shaped bands is observed by locating the peak positions at higher E_B in the momentum distribution curves (MDCs), and the energy at which these peaks merge is obtained by extrapolating linear fits to the MDCs. Therefore 50 meV represents a lower bound on the energy gap Δ between L_a and L_s . The magnitude of the extracted band velocities along the k_x and k_y directions are $7.9 \pm 0.5 \times 10^4 \text{ms}^{-1}$ and $10.0 \pm 0.5 \times 10^5 \text{ms}^{-1}$, respectively, which are similar to the tight binding values $7.6 \times 10^4 \text{ms}^{-1}$ and $9.1 \times 10^5 \text{ms}^{-1}$ calculated for the L_a band of bismuth [25]. Our data are consistent with the extremely small effective mass of $0.002m_e$ (where m_e is the electron mass) observed in magneto-reflection measurements on samples with $x = 11\%$ [29]. The Dirac point in graphene, coincidentally, has a band velocity ($|v_F| \approx 10^6 \text{ms}^{-1}$) [30] comparable to what we observe for $\text{Bi}_{0.9}\text{Sb}_{0.1}$, but its spin-orbit coupling is several orders of magnitude weaker, and the only known method of inducing a gap in the Dirac spectrum of graphene is by coupling to an external chemical substrate [31]. The $\text{Bi}_{1-x}\text{Sb}_x$ series thus provides a rare opportunity to study relativistic Dirac Hamiltonian physics in a 3D condensed matter system where the intrinsic (rest) mass gap can be easily tuned.

Studying the band dispersion perpendicular to the sample surface provides a way to differentiate bulk states from surface states in a 3D material. To visualize the near- E_F dispersion along the 3D L-X cut (X is a point that is displaced from L by a k_z distance of $3\pi/c$, where c is the lattice constant), in Fig.2a we plot energy distribution curves (EDCs), taken such that electrons at E_F have fixed in-plane momentum $(k_x, k_y) = (L_x, L_y) = (0.8 \text{Å}^{-1}, 0.0 \text{Å}^{-1})$, as a function of photon energy ($h\nu$). There are three prominent features in the EDCs: a non-dispersing, k_z independent, peak centered just below E_F at about -0.02eV ; a broad non-dispersing hump centered near -0.3eV ; and a strongly dispersing hump that coincides with the latter near $h\nu = 29 \text{eV}$. To understand which bands these features originate from, we show ARPES intensity maps along an in-plane cut $\bar{K}\bar{M}\bar{K}$ (parallel to the k_y direction) taken using $h\nu$ values of 22 eV, 29 eV and 35 eV, which correspond to approximate k_z values of $L_z - 0.3 \text{Å}^{-1}$, L_z , and $L_z + 0.3 \text{Å}^{-1}$ respectively (Fig.2b). At $h\nu = 29 \text{eV}$, the low energy ARPES spectral weight reveals a clear Λ -shaped band close to E_F . As the photon

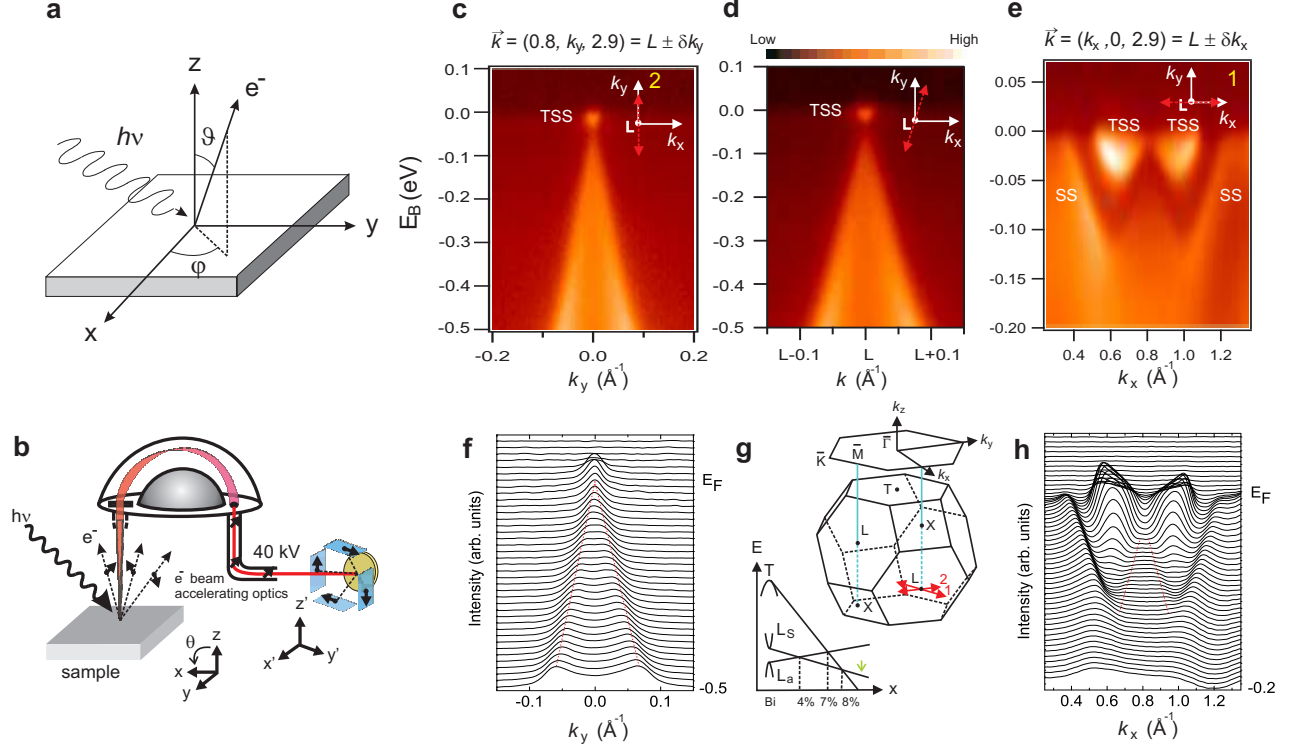


FIG. 2: The first 3D topological insulator (2007): Dirac-like dispersion signalling band inversion via spin-orbit interaction **a**, Schematic of an ARPES experimental geometry. The kinetic energy of photoelectrons and their angles of emission (θ, ϕ) determine its electronic structure. **b**, Energy and momentum analysis take place through a hemispherical analyzer and the spin analysis is performed using a Mott detector. Selected ARPES intensity maps of $\text{Bi}_{0.9}\text{Sb}_{0.1}$ are shown along three \vec{k} -space cuts through the L point of the bulk 3D Brillouin zone (BZ). The presented data are taken in the third BZ with $L_z = 2.9 \text{ \AA}^{-1}$ with a photon energy of 29 eV. The cuts are along **c**, the k_y direction, **d**, a direction rotated by approximately 10° from the k_y direction, and **e**, the k_x direction. Each cut shows a Λ -shaped bulk band whose tip lies below the Fermi level signalling a bulk gap. The (topological) surface states are denoted (T)SS and are all identified in Fig.3 [for further identification via theoretical calculations see Supplementary Materials (SM)]. **f**, Momentum distribution curves (MDCs) corresponding to the intensity map in **e**. **h**, Log scale plot of the MDCs corresponding to the intensity map in **e**. The red lines are guides to the eye for the bulk features in the MDCs. **g**, Schematic of the bulk 3D BZ of $\text{Bi}_{1-x}\text{Sb}_x$ and the 2D BZ of the projected (111) surface. The high symmetry points $\bar{\Gamma}$, \bar{M} and \bar{K} of the surface BZ are labeled. Schematic evolution of bulk band energies as a function of x is shown. The L band inversion transition occurs at $x \approx 0.04$, where a 3D gapless Dirac point is realized, and the composition we study here (for which $x = 0.1$) is indicated by the green arrow. A more detailed phase diagram based on our experiments is shown in Fig.4c. [Adapted from D. Hsieh *et al.*, *Nature* **452**, 970 (2008) (Completed and Submitted in **2007**) [14]].

energy is either increased or decreased from 29 eV, this intensity shifts to higher binding energies as the spectral weight evolves from the Λ -shaped into a \cup -shaped band. Therefore the dispersive peak in Fig.2a comes from the bulk valence band, and for $h\nu = 29$ eV the high symmetry point $L = (0.8, 0, 2.9)$ appears in the third bulk BZ. In the maps of Fig.2b with respective $h\nu$ values of 22 eV and 35 eV, overall weak features near E_F that vary in intensity remain even as the bulk valence band moves far below E_F . The survival of these weak features over a large photon energy range (17 to 55 eV) supports their surface origin. The non-dispersing feature centered near -0.3 eV in Fig.2a comes from the higher binding

energy (valence band) part of the full spectrum of surface states, and the weak non-dispersing peak at -0.02 eV reflects the low energy part of the surface states that cross E_F away from the \bar{M} point and forms the surface Fermi surface (Fig.2c).

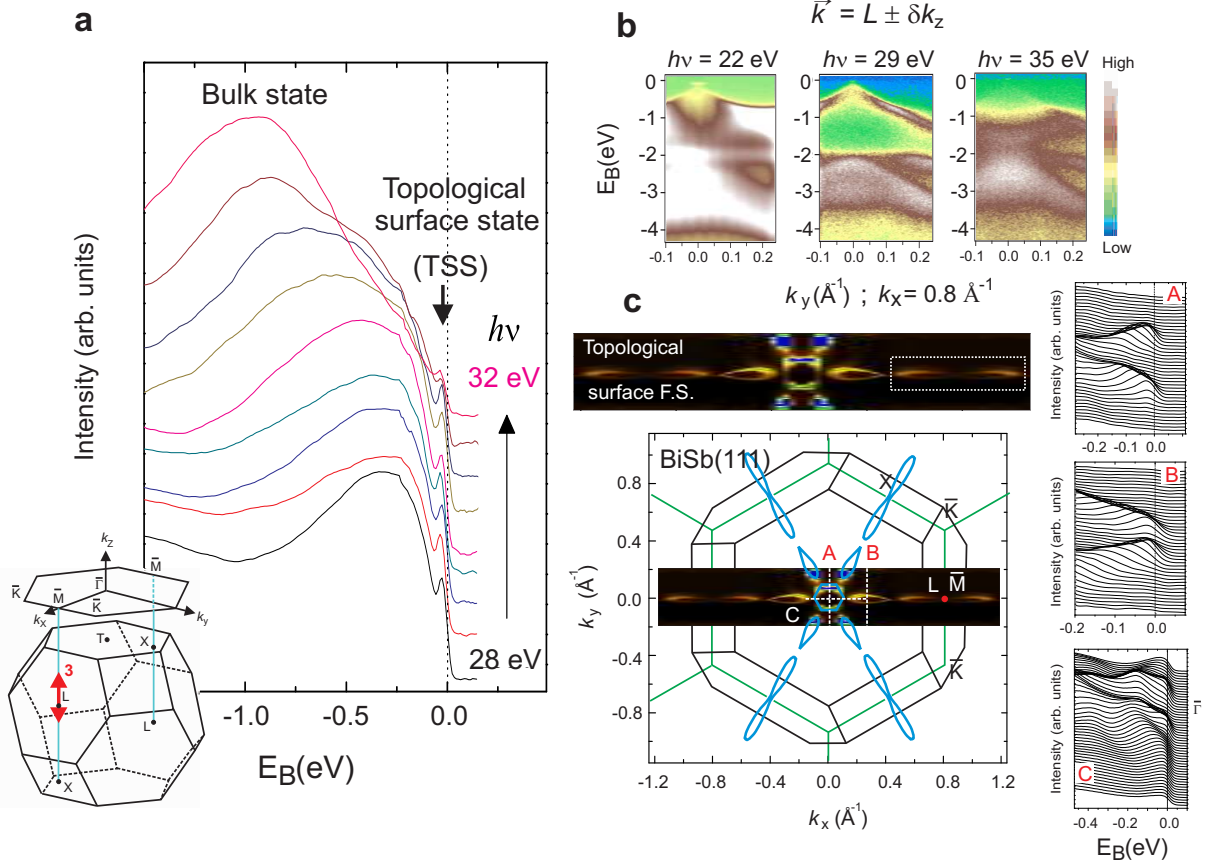


FIG. 3: The first 3D topological insulator (2007): Topological Surface States and electronic band dispersion along the k_z -direction in momentum space. Surface states are experimentally identified by studying their out-of-plane momentum dispersion through the systematic variation of incident photon energy. **a**, Energy distribution curves (EDCs) of $\text{Bi}_{0.9}\text{Sb}_{0.1}$ with electrons at the Fermi level (E_F) maintained at a fixed in-plane momentum of ($k_x=0.8 \text{ \AA}^{-1}$, $k_y=0.0 \text{ \AA}^{-1}$) are obtained as a function of incident photon energy to identify states that exhibit no dispersion perpendicular to the (111)-plane along the direction shown by the double-headed arrow labeled “3” in the inset (see SM). Selected EDC data sets with photon energies of 28 eV to 32 eV in steps of 0.5 eV are shown for clarity. The non-energy dispersive (k_z independent) peaks near E_F are the topological surface states (TSS). **b**, ARPES intensity maps along cuts parallel to k_y taken with electrons at E_F fixed at $k_x = 0.8 \text{ \AA}^{-1}$ with respective photon energies of $h\nu = 22 \text{ eV}$, 29 eV and 35 eV (for a conversion map from photon energy to k_z see SM). The faint Λ -shaped band at $h\nu = 22 \text{ eV}$ and $h\nu = 35 \text{ eV}$ shows some overlap with the bulk valence band at L ($h\nu = 29 \text{ eV}$), suggesting that it is a resonant surface state degenerate with the bulk state in some limited k -range near E_F . The flat band of intensity centered about -2 eV in the $h\nu = 22 \text{ eV}$ scan originates from Bi 5d core level emission from second order light. **c**, Projection of the bulk BZ (black lines) onto the (111) surface BZ (green lines). Overlay (enlarged in inset) shows the high resolution Fermi surface (FS) of the metallic SS mode, which was obtained by integrating the ARPES intensity (taken with $h\nu = 20 \text{ eV}$) from -15 meV to 10 meV relative to E_F . The six tear-drop shaped lobes of the surface FS close to $\bar{\Gamma}$ (center of BZ) show some intensity variation between them that is due to the relative orientation between the axes of the lobes and the axis of the detector slit. The six-fold symmetry was however confirmed by rotating the sample in the $k_x - k_y$ plane. EDCs corresponding to the cuts A, B and C are also shown; these confirm the gapless character of the surface states in bulk insulating $\text{Bi}_{0.9}\text{Sb}_{0.1}$. [Adapted from D. Hsieh *et al.*, *Nature* **452**, 970 (2008) (Completed and Submitted in **2007**)[14]].

WINDING NUMBER COUNT: COUNTING OF SURFACE FERMİ SURFACES ENCLOSING KRAMERS POINTS TO IDENTIFY TOPOLOGICALLY NON-TRIVIAL SURFACE SPIN-TEXTURED STATES

Having established the existence of an energy gap in the bulk state of $\text{Bi}_{0.9}\text{Sb}_{0.1}$ (Figs 1 and 2) and observed

linearly dispersive bulk bands uniquely consistent with strong spin-orbit coupling model calculations [25–28] (see SM for full comparison with theoretical calculation), we now discuss the topological character of its surface states, which are found to be gapless (Fig.2c). In general, the states at the surface of spin-orbit coupled compounds are allowed to be spin split owing to the loss of space inversion symmetry [$E(k, \uparrow) = E(-k, \uparrow)$]. However, as

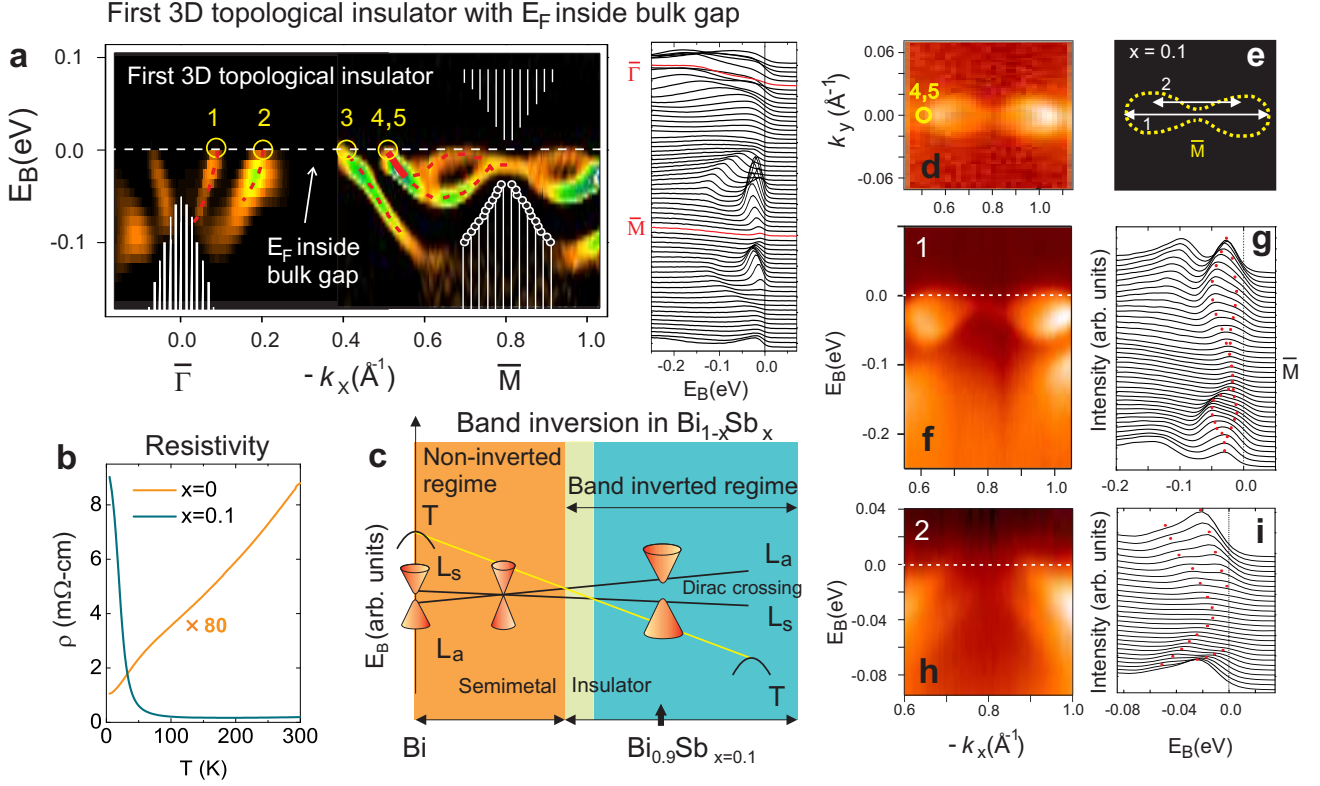


FIG. 4: The first 3D topological insulator (2007): The topological gapless surface states in bulk insulating (observed via the bulk band dispersion gap) $\text{Bi}_{0.9}\text{Sb}_{0.1}$. **a**, The surface band dispersion second derivative image (SDI) of $\text{Bi}_{0.9}\text{Sb}_{0.1}$ along $\bar{\Gamma} - \bar{M}$. The shaded white area shows the projection of the bulk bands based on ARPES data, as well as a rigid shift of the tight binding bands to sketch the unoccupied bands above the Fermi level. To maintain high momentum resolution, data were collected in two segments of momentum space, then the intensities were normalized using background level above the Fermi level. A non-intrinsic flat band of intensity near E_F generated by the SDI analysis was rejected to isolate the intrinsic dispersion. The Fermi crossings of the surface state are denoted by yellow circles, with the band near $-k_x \approx 0.5 \text{ \AA}^{-1}$ counted twice owing to double degeneracy. The red lines are guides to the eye. An in-plane rotation of the sample by 60° produced the same surface state dispersion. The EDCs along $\bar{\Gamma} - \bar{M}$ are shown to the right. There are a total of five crossings from $\bar{\Gamma} - \bar{M}$ which indicates that these surface states are topologically non-trivial. The number of surface state crossings in a material (with an odd number of Dirac points) is related to the topological Z_2 invariant (see text). **b**, The resistivity curves of Bi and $\text{Bi}_{0.9}\text{Sb}_{0.1}$ reflect the contrasting transport behaviours. The presented resistivity curve for pure bismuth has been multiplied by a factor of 80 for clarity. **c**, Schematic variation of bulk band energies of $\text{Bi}_{1-x}\text{Sb}_x$ as a function of x (based on band calculations and on [10, 24]). $\text{Bi}_{0.9}\text{Sb}_{0.1}$ is a direct gap bulk Dirac point insulator well inside the inverted-band regime, and its surface forms a “topological metal” - the 2D analogue of the 1D edge states in quantum spin Hall systems. **d**, ARPES intensity integrated within ± 10 meV of E_F originating solely from the surface state crossings. The image was plotted by stacking along the negative k_x direction a series of scans taken parallel to the k_y direction. **e**, Outline of $\text{Bi}_{0.9}\text{Sb}_{0.1}$ surface state ARPES intensity near E_F measured in **d**. White lines show scan directions “1” and “2”. **f**, Surface band dispersion along direction “1” taken with $h\nu = 28$ eV and the corresponding EDCs (**g**). The surface Kramers degenerate point, critical in determining the topological Z_2 class of a band insulator, is clearly seen at \bar{M} , approximately 15 ± 5 meV below E_F . (We note that the scans are taken along the negative k_x direction, away from the bulk L point.) **h**, Surface band dispersion along direction “2” taken with $h\nu = 28$ eV and the corresponding EDCs (**i**). This scan no longer passes through the \bar{M} -point, and the observation of two well separated bands indicates the absence of Kramers degeneracy as expected, which cross-checks the result in (**a**). [Adapted from D. Hsieh *et al.*, *Nature* **452**, 970 (2008) (Completed and Submitted in **2007**)[14]].

required by Kramers’ theorem, this splitting must go to zero at the four time reversal invariant momenta (TRIM) in the 2D surface BZ. As discussed in [10, 12], along a path connecting two TRIM in the same BZ, the Fermi energy inside the bulk gap will intersect these singly degenerate surface states either an even or odd number of

times. When there are an even number of surface state crossings, the surface states are topologically trivial because weak disorder (as may arise through alloying) or correlations can remove *pairs* of such crossings by pushing the surface bands entirely above or below E_F . When there are an odd number of crossings, however, at least

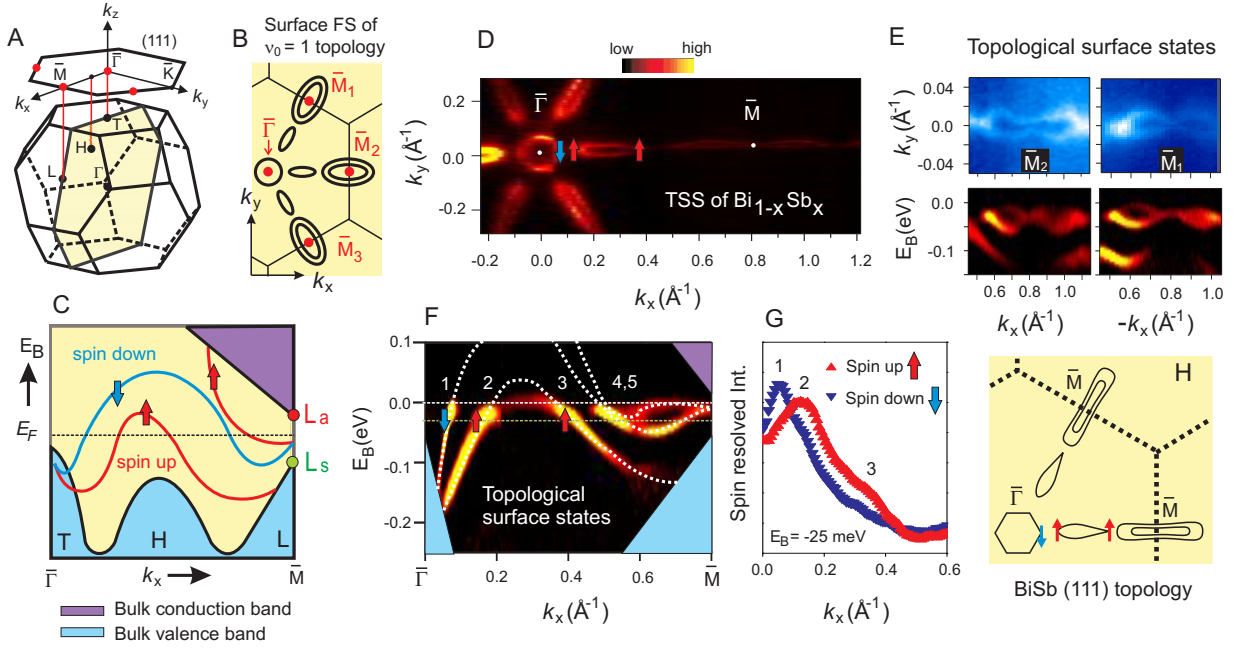


FIG. 5: **Spin texture of a topological insulator encodes Z_2 topological order of the bulk** (A) Schematic sketches of the bulk Brillouin zone (BZ) and (111) surface BZ of the $\text{Bi}_{1-x}\text{Sb}_x$ crystal series. The high symmetry points ($L, H, T, \Gamma, \bar{\Gamma}, \bar{M}, \bar{K}$) are identified. (B) Schematic of Fermi surface pockets formed by the surface states (SS) of a topological insulator that carries a Berry's phase. (C) Partner switching band structure topology: Schematic of spin-polarized SS dispersion and connectivity between $\bar{\Gamma}$ and \bar{M} required to realize the FS pockets shown in panel-(B). L_a and L_s label bulk states at L that are antisymmetric and symmetric respectively under a parity transformation (see text). (D) Spin-integrated ARPES intensity map of the SS of $\text{Bi}_{0.91}\text{Sb}_{0.09}$ at E_F . Arrows point in the measured direction of the spin. (E) High resolution ARPES intensity map of the SS at E_F that enclose the \bar{M}_1 and \bar{M}_2 points. Corresponding band dispersion (second derivative images) are shown below. The left right asymmetry of the band dispersions are due to the slight offset of the alignment from the $\bar{\Gamma}$ - \bar{M}_1 (\bar{M}_2) direction. (F) Surface band dispersion image along the $\bar{\Gamma}$ - \bar{M} direction showing five Fermi level crossings. The intensity of bands 4,5 is scaled up for clarity (the dashed white lines are guides to the eye). The schematic projection of the bulk valence and conduction bands are shown in shaded blue and purple areas. (G) Spin-resolved momentum distribution curves presented at $E_B = -25$ meV showing single spin degeneracy of bands at 1, 2 and 3. Spin up and down correspond to spin pointing along the $+\hat{y}$ and $-\hat{y}$ direction respectively. (H) Schematic of the spin-polarized surface FS observed in our experiments. It is consistent with a $\nu_0 = 1$ topology (compare (B) and (H)). [Adapted from D. Hsieh *et al.*, *Science* **323**, 919 (2009) (Completed and Submitted in 2008)[16]].

one surface state must remain gapless, which makes it non-trivial [10, 12, 23]. The existence of such topologically non-trivial surface states can be theoretically predicted on the basis of the *bulk* band structure only, using the Z_2 invariant that is related to the quantum Hall Chern number [8]. Materials with band structures with $Z_2 = +1$ are ordinary Bloch band insulators that are topologically equivalent to the filled shell atomic insulator, and are predicted to exhibit an even number (including zero) of surface state crossings. Materials with bulk band structures with $Z_2 = -1$ on the other hand, which are expected to exist in rare systems with strong spin-orbit coupling acting as an internal quantizing magnetic field on the electron system [32], and inverted bands at an odd number of high symmetry points in their bulk 3D BZs, are predicted to exhibit an odd number of surface state crossings, precluding their adiabatic continuation to the atomic insulator [9–13, 23]. Such “topological quantum Hall metals” [11, 12] cannot be realized in a purely

2D electron gas system such as the one realized at the interface of GaAs/GaAlAs systems.

In our experimental case, namely the (111) surface of $\text{Bi}_{0.9}\text{Sb}_{0.1}$, the four TRIM are located at $\bar{\Gamma}$ and three \bar{M} points that are rotated by 60° relative to one another. Owing to the three-fold crystal symmetry ($A7$ bulk structure) and the observed mirror symmetry of the surface Fermi surface across $k_x = 0$ (Fig.2), these three \bar{M} points are equivalent (and we henceforth refer to them as a single point, \bar{M}). The mirror symmetry [$E(k_y) = E(-k_y)$] is also expected from time reversal invariance exhibited by the system. The complete details of the surface state dispersion observed in our experiments along a path connecting $\bar{\Gamma}$ and \bar{M} are shown in Fig.3a; finding this information is made possible by our experimental separation of surface states from bulk states. As for bismuth (Bi), two surface bands emerge from the bulk band continuum near $\bar{\Gamma}$ to form a central electron pocket and an adjacent hole lobe [33–35]. It has been established that these two

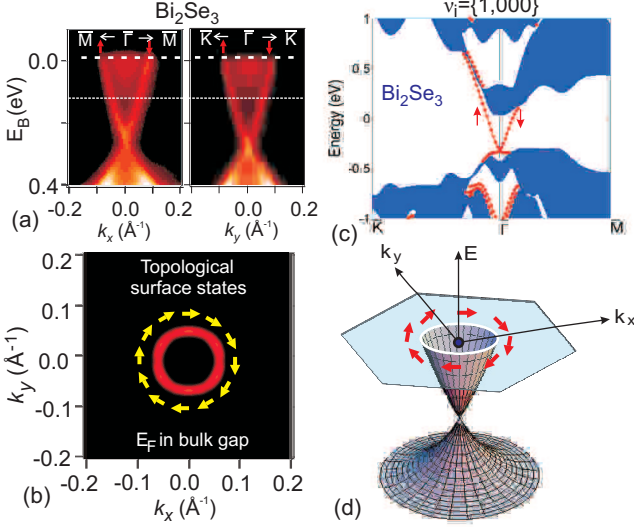


FIG. 6: Spin-momentum locked helical fermions reveal topological-order of the bulk: Spin-momentum locked helical surface Dirac fermions are hallmark signatures of topological insulators. (a) ARPES data for Bi₂Se₃ reveals surface electronic states with a single spin-polarized Dirac cone. The surface Fermi surface (b) exhibits a chiral left-handed spin texture. Data is from a sample doped to a Fermi level [thin line in (a)] that is in the bulk gap. (c) Surface electronic structure of Bi₂Se₃ computed in the local density approximation. The shaded regions describe bulk states, and the red lines are surface states. (d) Schematic of the spin polarized surface state dispersion in the Bi₂X₃ topological insulators. [Adapted from Y. Xia *et al.*, *Nature Phys.* **5**, 398 (2009). (Completed and Submitted in 2008) [15]].

bands result from the spin-splitting of a surface state and are thus singly degenerate [35, 36]. On the other hand, the surface band that crosses E_F at $-k_x \approx 0.5 \text{ \AA}^{-1}$, and forms the narrow electron pocket around \bar{M} , is clearly doubly degenerate, as far as we can determine within our experimental resolution. This is indicated by its splitting below E_F between $-k_x \approx 0.55 \text{ \AA}^{-1}$ and \bar{M} , as well as the fact that this splitting goes to zero at \bar{M} in accordance with Kramers theorem. In semimetallic single crystal bismuth, only a single surface band is observed to form the electron pocket around \bar{M} [37, 38]. Moreover, this surface state overlaps, hence becomes degenerate with, the bulk conduction band at L (L projects to the surface \bar{M} point) owing to the semimetallic character of Bi (Fig.3b). In Bi_{0.9}Sb_{0.1} on the other hand, the states near \bar{M} fall completely inside the bulk energy gap preserving their purely surface character at \bar{M} (Fig.3a). The surface Kramers doublet point can thus be defined in the bulk insulator (unlike in Bi [33–38]) and is experimentally located in Bi_{0.9}Sb_{0.1} samples to lie approximately $15 \pm 5 \text{ meV}$ below E_F at $\vec{k} = \bar{M}$ (Fig.3a). For the precise location of this Kramers point, it is important to demonstrate that our alignment is strictly along

the $\bar{\Gamma} - \bar{M}$ line. To do so, we contrast high resolution ARPES measurements taken along the $\bar{\Gamma} - \bar{M}$ line with those that are slightly offset from it (Fig.3e). Figs 3f-i show that with k_y offset from the Kramers point at \bar{M} by less than 0.02 \AA^{-1} , the degeneracy is lifted and only one band crosses E_F to form part of the bow-shaped electron distribution (Fig.3d). Our finding of five surface state crossings (an odd rather than an even number) between $\bar{\Gamma}$ and \bar{M} (Fig.3a), confirmed by our observation of the Kramers degenerate point at the TRIM, indicates that these gapless surface states are topologically non-trivial. This corroborates our bulk electronic structure result that Bi_{0.9}Sb_{0.1} is in the insulating band-inverted ($Z_2 = -1$) regime (Fig.3c), which contains an odd number of bulk (gapped) Dirac points, and is topologically analogous to an integer quantum spin Hall insulator.

Our experimental results taken collectively strongly suggest that Bi_{0.9}Sb_{0.1} is quite distinct from graphene [30, 39] and represents a novel state of quantum matter: a strongly spin-orbit coupled insulator with an odd number of Dirac points with a negative Z_2 topological Hall phase, which realizes the “parity anomaly without Fermion doubling”. Our work further demonstrates a general methodology for possible future investigations of *novel topological orders* in exotic quantum matter.

SPIN-RESOLVING THE SURFACE STATES TO IDENTIFY THE NON-TRIVIAL TOPOLOGICAL PHASE AND ESTABLISH A 2D HELICAL METAL PROTECTED FROM BACKSCATTERING

Strong topological materials are distinguished from ordinary materials such as gold by a topological quantum number, $\nu_0 = 1$ or 0 respectively [8, 11]. For Bi_{1-x}Sb_x, theory has shown that ν_0 is determined solely by the character of the bulk electronic wave functions at the L point in the three-dimensional (3D) Brillouin zone (BZ). When the lowest energy conduction band state is composed of an antisymmetric combination of atomic p -type orbitals (L_a) and the highest energy valence band state is composed of a symmetric combination (L_s), then $\nu_0 = 1$, and vice versa for $\nu_0 = 0$ [10]. Although the bonding nature (parity) of the states at L is not revealed in a measurement of the bulk band structure, the value of ν_0 can be determined from the spin-textures of the surface bands that form when the bulk is terminated. In particular, a $\nu_0 = 1$ topology requires the terminated surface to have a Fermi surface (FS) that supports a non-zero Berry’s phase (odd as opposed to even multiple of π), which is not realizable in an ordinary spin-orbit material.

In a general inversion symmetric spin-orbit insulator, the bulk states are spin degenerate because of a combination of space inversion symmetry [$E(\vec{k}, \uparrow) = E(-\vec{k}, \uparrow)$] and time reversal symmetry [$E(\vec{k}, \uparrow) = E(-\vec{k}, \downarrow)$]. Because space inversion symmetry is broken at the terminated surface, the spin degeneracy of surface bands can

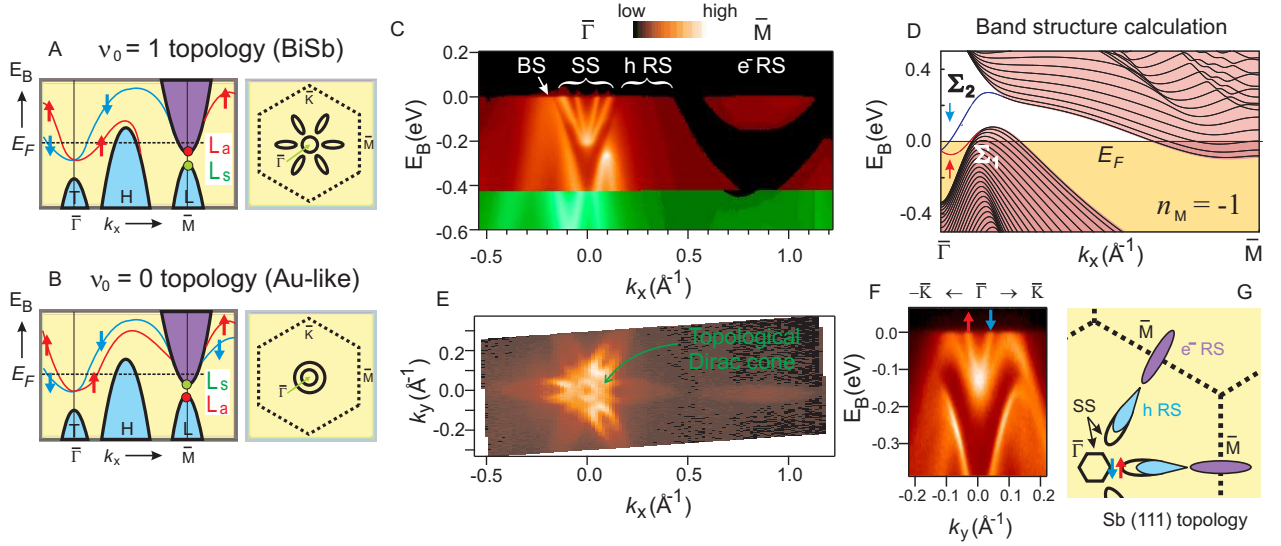


FIG. 7: Topological character of parent compound revealed on the (111) surface states. Schematic of the bulk band structure (shaded areas) and surface band structure (red and blue lines) of Sb near E_F for a (A) topologically non-trivial and (B) topological trivial (gold-like) case, together with their corresponding surface Fermi surfaces are shown. (C) Spin-integrated ARPES spectrum of Sb(111) along the $\bar{\Gamma}$ - \bar{M} direction. The surface states are denoted by SS, bulk states by BS, and the hole-like resonance states and electron-like resonance states by hRS and e^- RS respectively. (D) Calculated surface state band structure of Sb(111) based on the methods in [25, 40]. The continuum bulk energy bands are represented with pink shaded regions, and the lines show the discrete bands of a 100 layer slab. The red and blue single bands, denoted Σ_1 and Σ_2 , are the surface states bands with spin polarization $\langle \vec{P} \rangle \propto +\hat{y}$ and $\langle \vec{P} \rangle \propto -\hat{y}$ respectively. (E) ARPES intensity map of Sb(111) at E_F in the k_x - k_y plane. The only one FS encircling $\bar{\Gamma}$ seen in the data is formed by the inner V-shaped SS band seen in panel-(C) and (F). (F) ARPES spectrum of Sb(111) along the $\bar{\Gamma}$ - \bar{K} direction shows that the outer V-shaped SS band merges with the bulk band. (G) Schematic of the surface FS of Sb(111) showing the pockets formed by the surface states (unfilled) and the resonant states (blue and purple). The purely surface state Fermi pocket encloses only one Kramers degenerate point (\vec{k}_T), namely, $\bar{\Gamma}(=\vec{k}_T)$, therefore consistent with the $\nu_0 = 1$ topological classification of Sb which is different from Au (compare (B) and (G)). As discussed in the text, the hRS and e^- RS count trivially. [Adapted from D. Hsieh *et al.*, *Science* **323**, 919 (2009) (Completed and Submitted in 2008) [16]].

be lifted by the spin-orbit interaction [19-21]. However, according to Kramers theorem [16], they must remain spin degenerate at four special time reversal invariant momenta ($\vec{k}_T = \bar{\Gamma}, \bar{M}$) in the surface BZ [11], which for the (111) surface of $\text{Bi}_{1-x}\text{Sb}_x$ are located at $\bar{\Gamma}$ and three equivalent \bar{M} points [see Fig.5(A)].

Depending on whether ν_0 equals 0 or 1, the Fermi surface pockets formed by the surface bands will enclose the four \vec{k}_T an even or odd number of times respectively. If a Fermi surface pocket does not enclose \vec{k}_T ($= \bar{\Gamma}, \bar{M}$), it is irrelevant for the topology [10, 40]. Because the wave function of a single electron spin acquires a geometric phase factor of π [43] as it evolves by 360° in momentum space along a Fermi contour enclosing a \vec{k}_T , an odd number of Fermi pockets enclosing \vec{k}_T in total implies a π geometrical (Berry's) phase [10]. In order to realize a π Berry's phase the surface bands must be spin-polarized and exhibit a partner switching [10] dispersion behavior between a pair of \vec{k}_T . This means that any pair of spin-polarized surface bands that are degenerate at $\bar{\Gamma}$ must not re-connect at \bar{M} , or must separately connect to the bulk valence and conduction band in between $\bar{\Gamma}$ and \bar{M} . The partner switching behavior is realized in Fig.

5(C) because the spin down band connects to and is degenerate with different spin up bands at $\bar{\Gamma}$ and \bar{M} . The partner switching behavior is realized in Fig. 7(A) because the spin up and spin down bands emerging from $\bar{\Gamma}$ separately merge into the bulk valence and conduction bands respectively between $\bar{\Gamma}$ and \bar{M} .

We first investigate the spin properties of the topological insulator phase [16]. Spin-integrated ARPES [41] intensity maps of the (111) surface states of insulating $\text{Bi}_{1-x}\text{Sb}_x$ taken at the Fermi level (E_F) [Figs 5(D)&(E)] show that a hexagonal FS encloses $\bar{\Gamma}$, while dumbbell shaped FS pockets that are much weaker in intensity enclose \bar{M} . By examining the surface band dispersion below the Fermi level [Fig.5(F)] it is clear that the central hexagonal FS is formed by a single band (Fermi crossing 1) whereas the dumbbell shaped FSs are formed by the merger of two bands (Fermi crossings 4 and 5) [14].

This band dispersion resembles the partner switching dispersion behavior characteristic of topological insulators. To check this scenario and determine the topological index ν_0 , we have carried out spin-resolved photoemission spectroscopy. Fig.5(G) shows a spin-resolved momentum distribution curve taken along the $\bar{\Gamma}$ - \bar{M} direction at a binding energy $E_B = -25$ meV [Fig.5(G)]. The

Band inversion

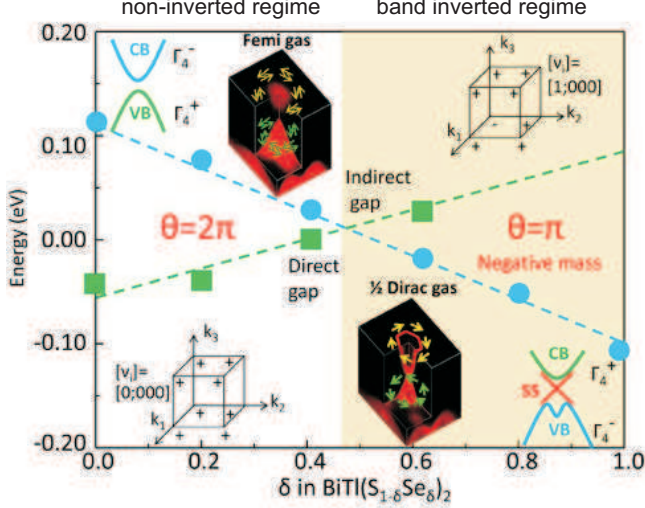


FIG. 8: **Observation of bulk band inversion across a topological quantum phase transition.** Energy levels of Γ_4^- (blue circles) and Γ_4^+ (green squares) bands are obtained from ARPES measurements as a function of composition δ . CB: conduction band; VB: valence band. Parity eigenvalues (+ or -) of Bloch states are shown. The topological invariants, ν_i , obtained from the parity eigenvalues are presented as $[\theta/\pi = \nu_0; \nu_1, \nu_2, \nu_3]$ where $\theta = \pi\nu_0$ is the axion angle [44] and ν_0 is the strong invariant. [Adapted from S.-Y. Xu *et al.*, *Science* **332** 560 (2011). [50]]

data reveal a clear difference between the spin-up and spin-down intensities of bands 1, 2 and 3, and show that bands 1 and 2 have opposite spin whereas bands 2 and 3 have the same spin (detailed analysis discussed later in text). The former observation confirms that bands 1 and 2 form a spin-orbit split pair, and the latter observation suggests that bands 2 and 3 (as opposed to bands 1 and 3) are connected above the Fermi level and form one band. This is further confirmed by directly imaging the bands through raising the chemical potential via doping (SM). Irrelevance of bands 2 and 3 to the topology is consistent with the fact that the Fermi surface pocket they form does not enclose any \vec{k}_T . Because of a dramatic intrinsic weakening of signal intensity near crossings 4 and 5, and the small energy and momentum splitting of bands 4 and 5 lying at the resolution limit of modern spin-resolved ARPES spectrometers, no conclusive spin information about these two bands can be drawn from the methods employed in obtaining the data sets in Figs 5(G)&(H). However, whether bands 4 and 5 are both singly or doubly degenerate does not change the fact that an odd number of spin-polarized FSs enclose the \vec{k}_T , which provides evidence that $\text{Bi}_{1-x}\text{Sb}_x$ has $\nu_0 = 1$ and that its surface supports a non-trivial Berry's phase. This directly implies an absence of backscattering in electronic transport along the surface (Fig.11).

Shortly after the discovery of $\text{Bi}_{1-x}\text{Sb}_x$, physicists

sought to find a simpler version of a 3D topological insulator consisting of a single surface state instead of five. This is because the surface structure of $\text{Bi}_{1-x}\text{Sb}_x$ was rather complicated and the band gap was rather small. This motivated a search for topological insulators with a larger band gap and simpler surface spectrum. A second generation of 3D topological insulator materials, especially Bi_2Se_3 , offers the potential for topologically protected behavior in ordinary crystals at room temperature and zero magnetic field. Starting in 2008, work by the Princeton group used spin-ARPES and first-principles calculations to study the surface band structure of Bi_2Se_3 and observe the characteristic signature of a topological insulator in the form of a single Dirac cone that is spin-polarized (Figs 6 and 10) such that it also carries a non-trivial Berry's phase [15, 17]. Concurrent theoretical work by [19] used electronic structure methods to show that Bi_2Se_3 is just one of several new large band-gap topological insulators. These other materials were soon after also identified using this ARPES technique we describe [18, 20].

The Bi_2Se_3 surface state is found from spin-ARPES and theory to be a nearly idealized single Dirac cone as seen from the experimental data in Figs.6 and 14. An added advantage is that Bi_2Se_3 is stoichiometric (i.e., a pure compound rather than an alloy such as $\text{Bi}_{1-x}\text{Sb}_x$) and hence can be prepared, in principle, at higher purity. While the topological insulator phase is predicted to be quite robust to disorder, many experimental probes of the phase, including ARPES of the surface band structure, are clearer in high-purity samples. Finally and perhaps most important for applications, Bi_2Se_3 has a large band gap of around 0.3 eV (3600 K). This indicates that in its high-purity form Bi_2Se_3 can exhibit topological insulator behavior at room temperature and greatly increases the potential for applications, which we discuss in greater depth later in the review.

IDENTIFYING THE ORIGIN OF 3D TOPOLOGICAL ORDER VIA A BULK BAND GAP INVERSION TRANSITION

We investigated the quantum origin of topological order in this class of materials. It has been theoretically speculated that the novel topological order originates from the parities of the electrons in pure Sb and not Bi [10, 24]. It was also noted [40] that the origin of the topological effects can only be tested by measuring the spin-texture of the Sb surface, which has not been measured. Based on quantum oscillation and magneto-optical studies, the bulk band structure of Sb is known to evolve from that of insulating $\text{Bi}_{1-x}\text{Sb}_x$ through the hole-like band at H rising above E_F and the electron-like band at L sinking below E_F [24]. The relative energy ordering of the L_a and L_s states in Sb again determines whether the surface state pair emerging from $\bar{\Gamma}$ switches partners [Fig.7(A)] or not [Fig.7(B)] between $\bar{\Gamma}$ and \bar{M} , and in turn determines whether they support a non-zero

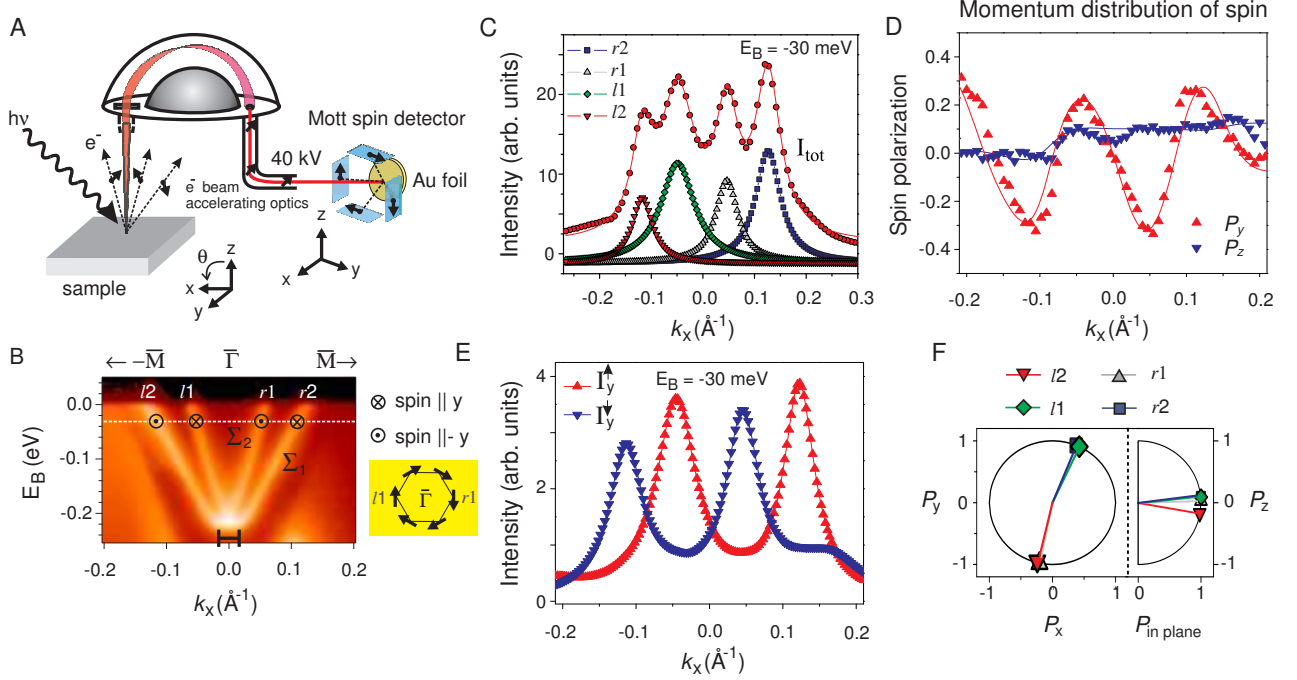


FIG. 9: **Spin-texture of topological surface states and topological chirality.** (A) Experimental geometry of the spin-resolved ARPES study. At normal emission ($\theta = 0^\circ$), the sensitive y' -axis of the Mott detector is rotated by 45° from the sample $\bar{\Gamma}$ to $-\bar{M}$ ($\parallel -\hat{x}$) direction, and the sensitive z' -axis of the Mott detector is parallel to the sample normal ($\parallel \hat{z}$). (B) Spin-integrated ARPES spectrum of Sb(111) along the $-\bar{M}-\bar{\Gamma}-\bar{M}$ direction. The momentum splitting between the band minima is indicated by the black bar and is approximately 0.03 \AA^{-1} . A schematic of the spin chirality of the central FS based on the spin-resolved ARPES results is shown on the right. (C) Momentum distribution curve of the spin averaged spectrum at $E_B = -30 \text{ meV}$ (shown in (B) by white line), together with the Lorentzian peaks of the fit. (D) Measured spin polarization curves (symbols) for the detector y' and z' components together with the fitted lines using the two-step fitting routine [45]. (E) Spin-resolved spectra for the sample y component based on the fitted spin polarization curves shown in (D). Up (down) triangles represent a spin direction along the $+\hat{y}$ ($-\hat{y}$) direction. (F) The in-plane and out-of-plane spin polarization components in the sample coordinate frame obtained from the spin polarization fit. Overall spin-resolved data and the fact that the surface band that forms the central electron pocket has $\langle P \rangle \propto -\hat{y}$ along the $+k_x$ direction, as in (E), suggest a left-handed chirality (schematic in (B) and see text for details). [Adapted from D. Hsieh *et al.*, *Science* **323**, 919 (2009) [16]].

Berry's phase.

In a conventional spin-orbit metal such as gold, a free-electron like surface state is split into two parabolic spin-polarized sub-bands that are shifted in \vec{k} -space relative to each other [46]. Two concentric spin-polarized Fermi surfaces are created, one having an opposite sense of in-plane spin rotation from the other, that enclose $\bar{\Gamma}$. Such a Fermi surface arrangement, like the schematic shown in figure 7(B), does not support a non-zero Berry's phase because the \vec{k}_T are enclosed an even number of times (2 for most known materials).

However, for Sb, this is not the case. Figure 7(C) shows a spin-integrated ARPES intensity map of Sb(111) from $\bar{\Gamma}$ to \bar{M} . By performing a systematic incident photon energy dependence study of such spectra, previously unavailable with He lamp sources [47], it is possible to identify two V-shaped surface states (SS) centered at $\bar{\Gamma}$, a bulk state located near $k_x = -0.25 \text{ \AA}^{-1}$ and resonance states centered about $k_x = 0.25 \text{ \AA}^{-1}$ and \bar{M} that are hybrid states formed by surface and bulk states [41]

(SM). An examination of the ARPES intensity map of the Sb(111) surface and resonance states at E_F [Fig.7(E)] reveals that the central surface FS enclosing $\bar{\Gamma}$ is formed by the inner V-shaped SS only. The outer V-shaped SS on the other hand forms part of a tear-drop shaped FS that does *not* enclose $\bar{\Gamma}$, unlike the case in gold. This tear-drop shaped FS is formed partly by the outer V-shaped SS and partly by the hole-like resonance state. The electron-like resonance state FS enclosing \bar{M} does not affect the determination of ν_0 because it must be doubly spin degenerate (SM). Such a FS geometry [Fig.7(G)] suggests that the V-shaped SS pair may undergo a partner switching behavior expected in Fig.7(A). This behavior is most clearly seen in a cut taken along the $\bar{\Gamma}-\bar{K}$ direction since the top of the bulk valence band is well below E_F [Fig.7(F)] showing only the inner V-shaped SS crossing E_F while the outer V-shaped SS bends back towards the bulk valence band near $k_x = 0.1 \text{ \AA}^{-1}$ before reaching E_F . The additional support for this band dispersion behavior comes from tight binding surface calculations

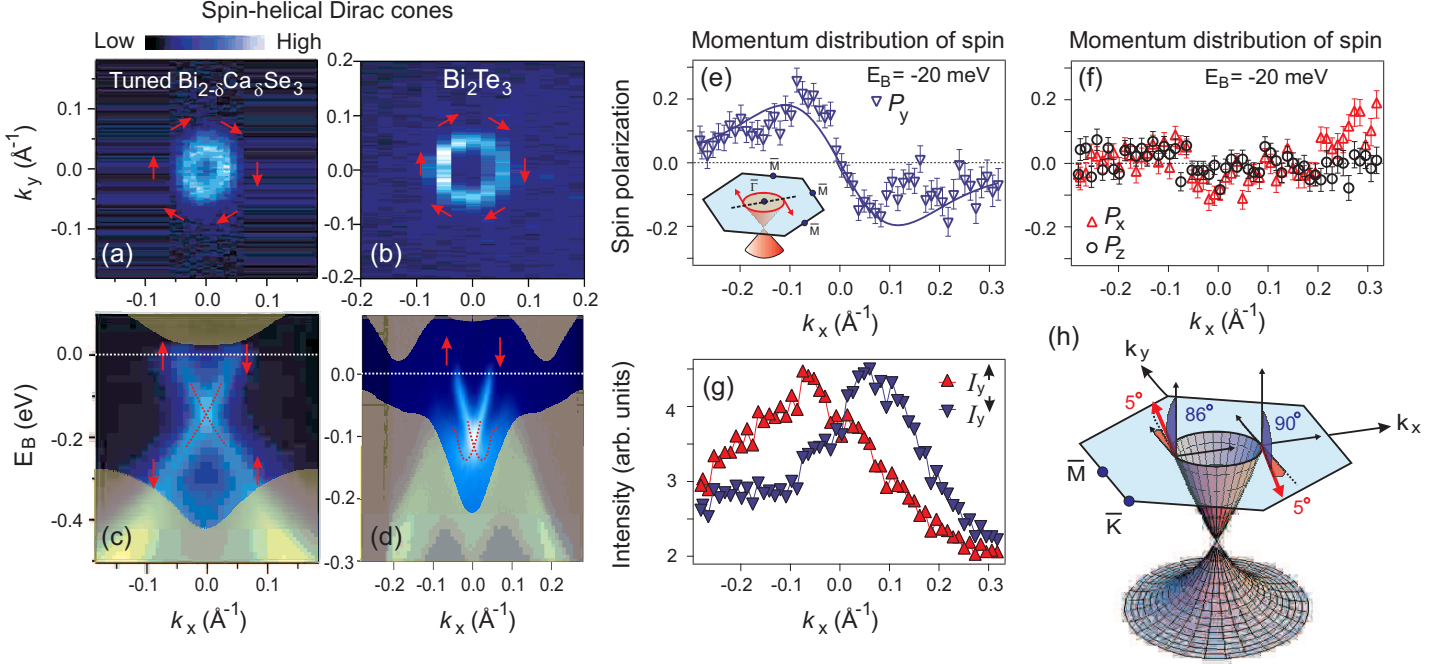


FIG. 10: **First detection of Topological-Order: spin-momentum locking of spin-helical Dirac electrons in Bi_2Se_3 and Bi_2Te_3 using spin-resolved ARPES.** (a) ARPES intensity map at E_F of the (111) surface of tuned $\text{Bi}_{2-\delta}\text{Ca}_\delta\text{Se}_3$ (see text) and (b) the (111) surface of Bi_2Te_3 . Red arrows denote the direction of spin around the Fermi surface. (c) ARPES dispersion of tuned $\text{Bi}_{2-\delta}\text{Ca}_\delta\text{Se}_3$ and (d) Bi_2Te_3 along the k_x cut. The dotted red lines are guides to the eye. The shaded regions in (c) and (d) are our calculated projections of the bulk bands of pure Bi_2Se_3 and Bi_2Te_3 onto the (111) surface respectively. (e) Measured y component of spin-polarization along the $\bar{\Gamma}$ - \bar{M} direction at $E_B = -20$ meV, which only cuts through the surface states. Inset shows a schematic of the cut direction. (f) Measured x (red triangles) and z (black circles) components of spin-polarization along the $\bar{\Gamma}$ - \bar{M} direction at $E_B = -20$ meV. Error bars in (e) and (f) denote the standard deviation of $P_{x,y,z}$, where typical detector counts reach 5×10^5 ; Solid lines are numerical fits [42]. (g) Spin-resolved spectra obtained from the y component spin polarization data. The non-Lorentzian lineshape of the I_y^{\uparrow} and I_y^{\downarrow} curves and their non-exact merger at large $|k_x|$ is due to the time evolution of the surface band dispersion, which is the dominant source of statistical uncertainty. a.u., arbitrary units. (h) Fitted values of the spin polarization vector $\mathbf{P} = (S_x, S_y, S_z)$ are $(\sin(90^\circ)\cos(-95^\circ), \sin(90^\circ)\sin(-95^\circ), \cos(90^\circ))$ for electrons with $+k_x$ and $(\sin(86^\circ)\cos(85^\circ), \sin(86^\circ)\sin(85^\circ), \cos(86^\circ))$ for electrons with $-k_x$, which demonstrates the topological helicity of the spin-Dirac cone. The angular uncertainties are of order $\pm 10^\circ$ and the magnitude uncertainty is of order ± 0.15 . [Adapted from D. Hsieh *et al.*, *Nature* **460**, 1101 (2009). [17]].

on Sb [Fig.7(D)], which closely match with experimental data below E_F . Our observation of a single surface band forming a FS enclosing $\bar{\Gamma}$ suggests that pure Sb is likely described by $\nu_0 = 1$, and that its surface may support a Berry's phase.

Confirmation of a surface π Berry's phase rests critically on a measurement of the relative spin orientations (up or down) of the SS bands near $\bar{\Gamma}$ so that the partner switching is indeed realized, which cannot be done without spin resolution. Spin resolution was achieved using a Mott polarimeter that measures two orthogonal spin components of a photoemitted electron [48, 49]. These two components are along the y' and z' directions of the Mott coordinate frame, which lie predominantly in and out of the sample (111) plane respectively. Each of these two directions represents a normal to a scattering plane defined by the photoelectron incidence direction

on a gold foil and two electron detectors mounted on either side (left and right) [Fig.9(A)]. Strong spin-orbit coupling of atomic gold is known to create an asymmetry in the scattering of a photoelectron off the gold foil that depends on its spin component normal to the scattering plane [49]. This leads to an asymmetry between the left intensity ($I_{y',z'}^L$) and right intensity ($I_{y',z'}^R$) given by $A_{y',z'} = (I_{y',z'}^L - I_{y',z'}^R)/(I_{y',z'}^L + I_{y',z'}^R)$, which is related to the spin polarization $P_{y',z'} = (1/S_{eff}) \times A_{y',z'}$ through the Sherman function $S_{eff} = 0.085$ [48, 49]. Spin-resolved momentum distribution curve data sets of the SS bands along the $-\bar{M}$ - $\bar{\Gamma}$ - \bar{M} cut at $E_B = -30$ meV [Fig.9(B)] are shown for maximal intensity. Figure 9(D) displays both y' and z' polarization components along this cut, showing clear evidence that the bands are spin polarized, with spins pointing largely in the (111) plane. In order to estimate the full 3D spin polarization vec-

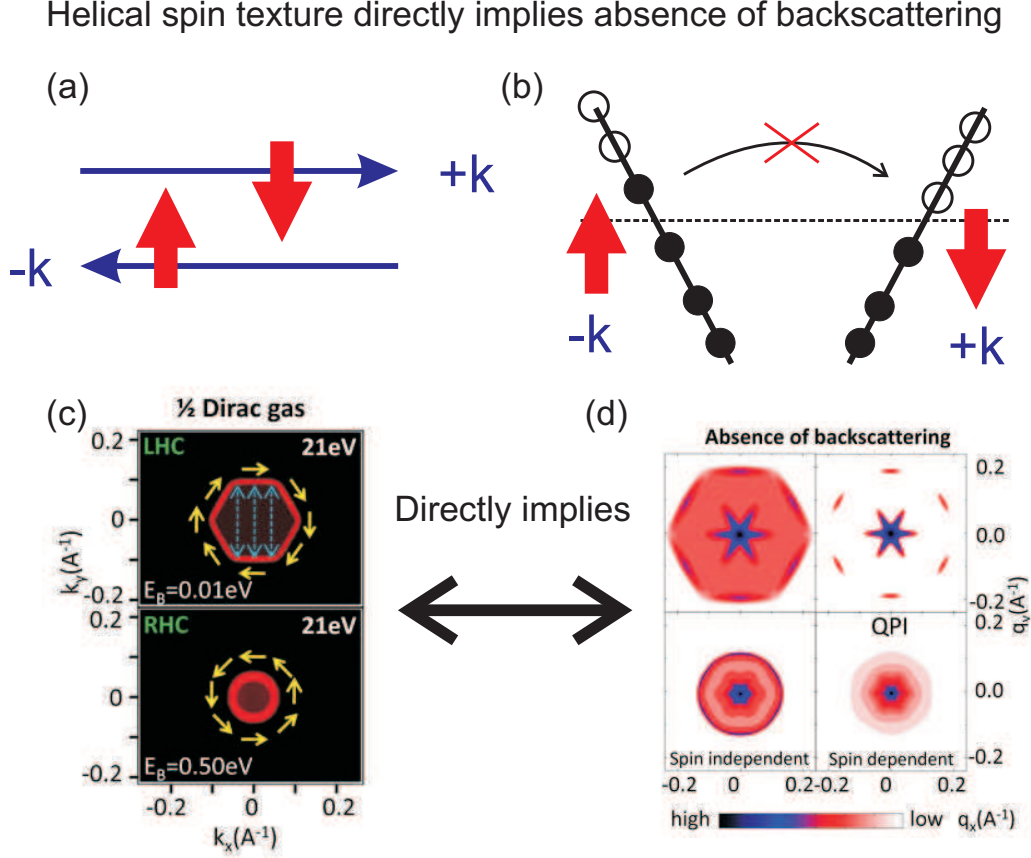


FIG. 11: Helical spin texture naturally leads to absence of elastic backscattering for surface transport: No "U" turn on a 3D topological insulator surface. (a) Our measurement of a helical spin texture in both $\text{Bi}_{1-x}\text{Sb}_x$ and in Bi_2Se_3 directly shows that there is (b) an absence of backscattering. (c) ARPES measured FSs are shown with spin directions based on polarization measurements. L(R)HC stands for left(right)-handed chirality. (d) Spin independent and spin dependent scattering profiles on FSs in (c) relevant for surface quasi-particle transport are shown which is sampled by the quasi-particle interference (QPI) modes. [Adapted from S.-Y. Xu *et al.*, *Science* **332** 560 (2011). [50]]

tors from a two component measurement (which is not required to prove the partner switching or the Berry's phase), we fit a model polarization curve to our data following the recent demonstration in Ref-[45], which takes the polarization directions associated with each momentum distribution curve peak [Fig.9(C)] as input parameters, with the constraint that each polarization vector has length one (in angular momentum units of $\hbar/2$). Our fitted polarization vectors are displayed in the sample (x, y, z) coordinate frame [Fig.9(F)], from which we derive the spin-resolved momentum distribution curves for the spin components parallel (I_y^\uparrow) and anti-parallel (I_y^\downarrow) to the y direction (SM) as shown in figure 9(E). There is a clear difference in I_y^\uparrow and I_y^\downarrow at each of the four momentum distribution curve peaks indicating that the surface state bands are spin polarized [Fig.9(E)], which is possible to conclude even without a full 3D fitting. Each of the pairs $l2/l1$ and $r1/r2$ have opposite spin, consistent with the behavior of a spin split pair, and the spin polarization of these bands are reversed on either side of $\bar{\Gamma}$ in ac-

cordance with the system being time reversal symmetric [$E(\vec{k}, \uparrow) = E(-\vec{k}, \downarrow)$] [Fig.9(F)]. The measured spin texture of the $\text{Sb}(111)$ surface states (Fig.9), together with the connectivity of the surface bands (Fig.7), uniquely determines its belonging to the $\nu_0 = 1$ class. Therefore the surface of Sb carries a non-zero (π) Berry's phase via the inner V-shaped band and pure Sb can be regarded as the parent metal of the $\text{Bi}_{1-x}\text{Sb}_x$ topological insulator class, in other words, the topological order originates from the Sb wave functions. A recent work [50] has demonstrated a topological quantum phase transition as a function of chemical composition from a non-inverted to an inverted semiconductor as a clear example of the origin of topological order (Fig.IV).

Our spin polarized measurement methods (Fig.5 and 9) uncover a new type of topological quantum number n_M which provides information about the chirality properties. Topological band theory suggests that the bulk electronic states in the mirror ($k_y = 0$) plane can be classified in terms of a number $n_M (= \pm 1)$ that describes

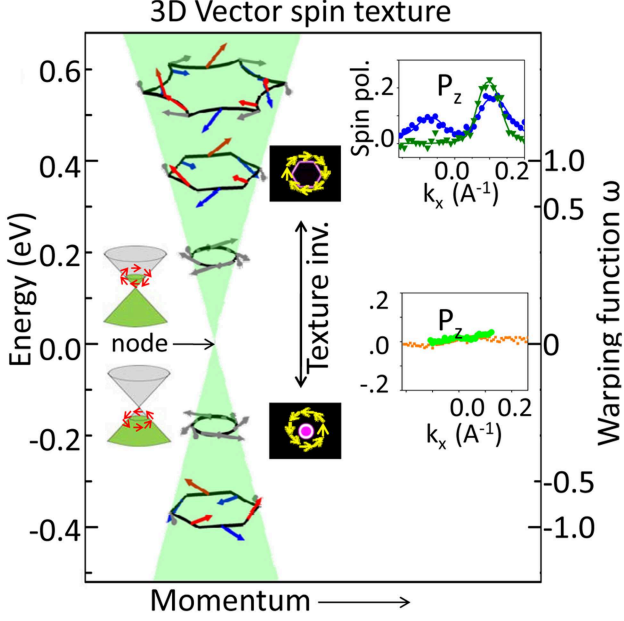


FIG. 12: **Spin texture evolution of topological surface bands as a function of energy away from the Dirac node** (left axis) and geometrical warping factor ω (right axis). The warping factor is defined as $\omega = \frac{k_F(\bar{\Gamma}-\bar{M}) - k_F(\bar{\Gamma}-\bar{K})}{k_F(\bar{\Gamma}-\bar{M}) + k_F(\bar{\Gamma}-\bar{K})} \times \frac{2+\sqrt{3}}{2-\sqrt{3}}$ where $\omega = 0$, $\omega = 1$, and $\omega > 1$ implies circular, hexagonal and snowflake-shaped FSs respectively. The sign of ω indicates texture chirality for LHC (+) or RHC (-). Insets: out-of-plane 3D spin-polarization measurements at corresponding FSs. [Adapted from S.-Y. Xu *et al.*, *Science* **332** 560 (2011). [50]]

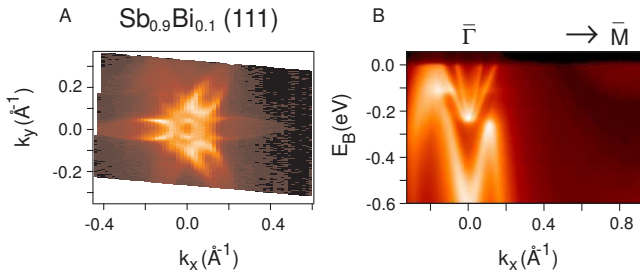


FIG. 13: **Robustness against disorder** Spin split surface states survive alloying disorder in $\text{Sb}_{0.9}\text{Bi}_{0.1}$. (A) ARPES intensity map at E_F of single crystal $\text{Sb}_{0.9}\text{Bi}_{0.1}$ (111) in the k_x - k_y plane taken using 20 eV photons. (B) ARPES intensity map of $\text{Sb}_{0.9}\text{Bi}_{0.1}$ (111) along the $\bar{\Gamma}$ - \bar{M} direction taken with $h\nu = 22$ eV photons. The band dispersion is not symmetric about $\bar{\Gamma}$ because of the three-fold rotational symmetry of the bulk states about the $\langle 111 \rangle$ axis. [Adapted from D. Hsieh *et al.*, *Science* **323**, 919 (2009) [16]].

the handedness (either left or right handed) or chirality of the surface spins which can be directly measured or seen in spin-resolved experiments [40]. We now determine the value of n_M from our data. From figure 5, it is seen that a single (one) surface band, which switches partners at \bar{M} , connects the bulk valence and conduction bands, so $|n_M| = 1$ (SM). The sign of n_M is related to the direction of the spin polarization $\langle \vec{P} \rangle$ of this band [40], which is constrained by mirror symmetry to point along $\pm \hat{y}$. Since the central electron-like FS enclosing $\bar{\Gamma}$ intersects six mirror invariant points [see Fig.9(B)], the sign of n_M distinguishes two distinct types of handedness for this spin polarized FS. Figures 5(F) and 9 show that for both $\text{Bi}_{1-x}\text{Sb}_x$ and Sb , the surface band that forms this electron pocket has $\langle \vec{P} \rangle \propto -\hat{y}$ along the k_x direction, suggesting a left-handed rotation sense for the spins around this central FS thus $n_M = -1$. Therefore, both insulating $\text{Bi}_{1-x}\text{Sb}_x$ and pure Sb possess equivalent chirality properties – a definite spin rotation sense (left-handed chirality, see Fig.9(B)) and a topological Berry's phase. Recently a chirality transition across the surface Dirac point of a 3D topological insulator has also been observed using spin-ARPES [50] (Fig.12).

These spin-resolved experimental measurements reveal an intimate and straightforward connection between the topological numbers (ν_0 , n_M) and the physical observables. The ν_0 determines whether the surface electrons support a non-trivial Berry's phase, and if they do, the n_M determines the spin handedness of the Fermi surface that manifests this Berry's phase. The 2D Berry's phase is a critical signature of topological order and is not realizable in isolated 2D electron systems, nor on the surfaces of conventional spin-orbit or exchange coupled magnetic materials. A non-zero Berry's phase is known, theoretically, to protect an electron system against the almost universal weak-localization behavior in their low temperature transport [10, 51] and is expected to form the key element for fault-tolerant computation schemes [51, 52], because the Berry's phase is a geometrical agent or mechanism for protection against quantum decoherence [53]. Its remarkable realization on the $\text{Bi}_{1-x}\text{Sb}_x$ surface represents an unprecedented example of a 2D π Berry's phase, and opens the possibility for building realistic prototype systems to test quantum computing modules. In general, our results demonstrate that spin-ARPES is a powerful probe of 3D topological order, which opens up a new search front for topological materials for novel spin-devices and fault-tolerant quantum computing.

TOPOLOGICAL PROTECTION AND TUNABILITY OF THE SURFACE STATES OF A 3D TOPOLOGICAL INSULATOR

The predicted topological protection of the surface states of Sb implies that their metallicity cannot be destroyed by weak time reversal symmetric perturbations. In order to test the robustness of the measured gapless

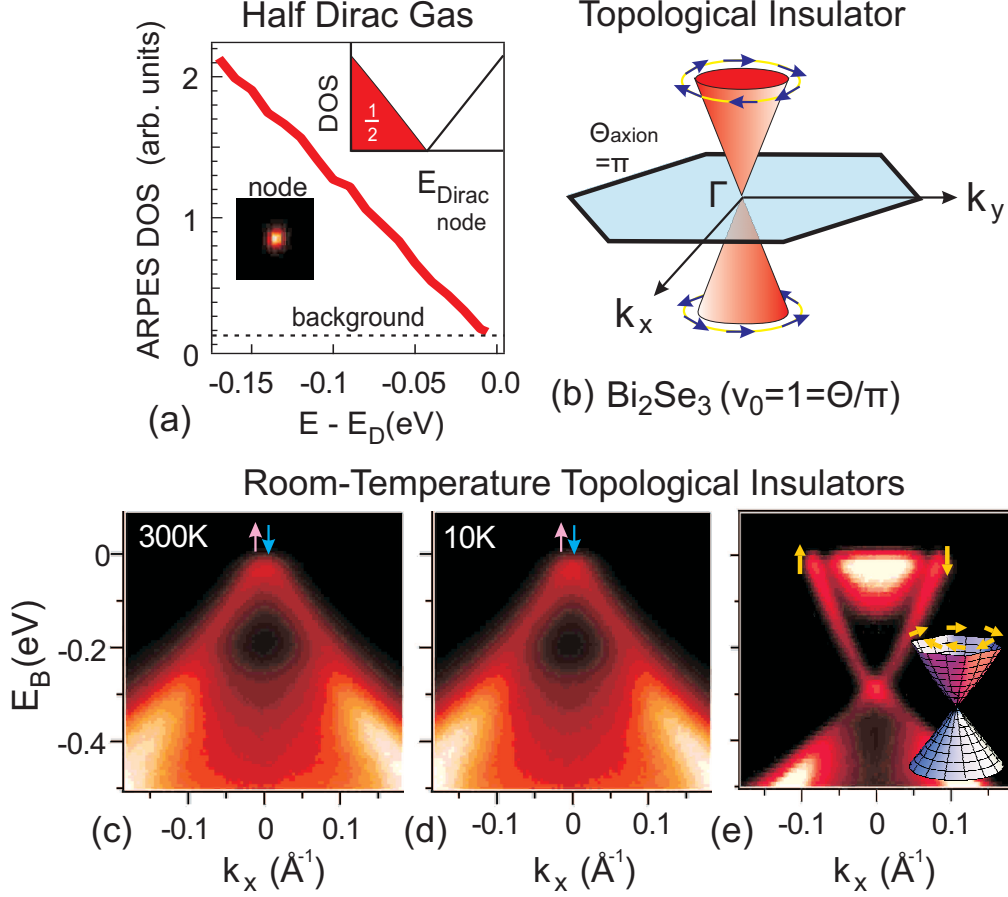


FIG. 14: **Observation of room temperature (300K) topological order without applied magnetic field in Bi_2Se_3 :** (a) Crystal momentum integrated ARPES data near Fermi level exhibit linear fall-off of density of states, which, combined with the spin-resolved nature of the states, suggest that a half Fermi gas is realized on the topological surfaces. (b) Spin texture map based on spin-ARPES data suggest that the spin-chirality changes sign across the Dirac point. (c) The Dirac node remains well defined up a temperature of 300 K suggesting the stability of topological effects up to the room temperature. (d) The Dirac cone measured at a temperature of 10 K. (e) Full Dirac cone. [Adapted from D. Hsieh *et al.*, *Nature* **460**, 1101 (2009). [17]].

surface states of Sb, we introduce such a perturbation by randomly substituting Bi into the Sb crystal matrix. Another motivation for performing such an experiment is that the formalism developed by Fu and Kane [10] to calculate the Z_2 topological invariants relies on inversion symmetry being present in the bulk crystal, which they assumed to hold true even in the random alloy $\text{Bi}_{1-x}\text{Sb}_x$. However, this formalism is simply a device for simplifying the calculation and the non-trivial $\nu_0 = 1$ topological class of $\text{Bi}_{1-x}\text{Sb}_x$ is predicted to hold true even in the absence of inversion symmetry in the bulk crystal [10]. Therefore introducing light Bi substitutional disorder into the Sb matrix is also a method to examine the effects of alloying disorder and possible breakdown of bulk inversion symmetry on the surface states of Sb(111). We have performed spin-integrated ARPES measurements on single crystals of the random alloy $\text{Sb}_{0.9}\text{Bi}_{0.1}$. Figure 13 shows that both the surface band dispersion along $\bar{\Gamma}$ - \bar{M} as well as the surface state Fermi surface retain the

same form as that observed in Sb(111), and therefore the ‘topological metal’ surface state of Sb(111) fully survives the alloy disorder. Since Bi alloying is seen to only affect the band structure of Sb weakly, it is reasonable to assume that the topological order is preserved between Sb and $\text{Bi}_{0.91}\text{Sb}_{0.09}$ as we observed.

In a simpler fashion compared to $\text{Bi}_{1-x}\text{Sb}_x$, the topological insulator behavior in Bi_2Se_3 is associated with a single band inversion at the surface Brillouin zone center. Owing to its larger bandgap compared with $\text{Bi}_{1-x}\text{Sb}_x$, ARPES has shown that its topological properties are preserved at room temperature [17]. Two defining properties of topological insulators—spin-momentum locking of surface states and π Berry phase—can be clearly demonstrated in the Bi_2Se_3 series. The surface states are expected to be protected by time-reversal symmetry, which implies that the surface Dirac node should be robust in the presence of nonmagnetic disorder but open a gap in the presence of time-reversal symmetry

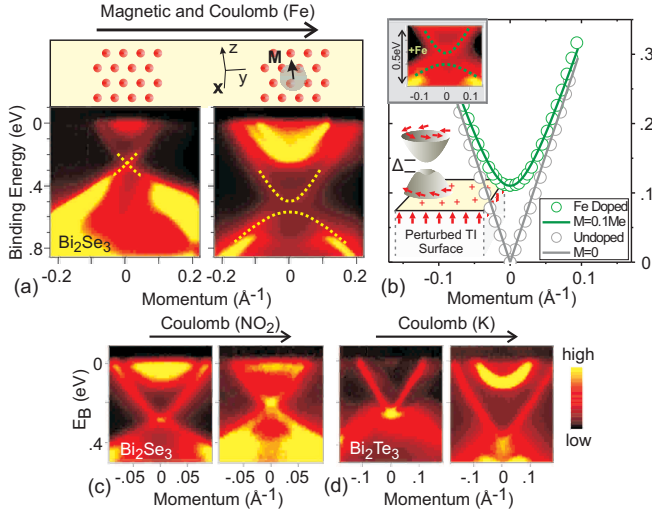


FIG. 15: **Protection by time reversal symmetry:** Topological surface states are robust in the presence of strong non-magnetic disorder but open a gap in the presence of time reversal symmetry breaking magnetic impurities and disorder. (a) Magnetic impurity such as Fe on the surface of Bi_2Se_3 opens a gap at the Dirac point. The magnitude of the gap is set by the interaction of Fe ions with the Se surface and the time reversal symmetry breaking disorder potential introduced on the surface. (b) A comparison of surface band dispersion with and without Fe doping. (c,d) Non-magnetic disorder created via molecular adsorbent NO_2 or alkali atom adsorption (K or Na) on the surface leaves the Dirac node intact in both Bi_2Se_3 and Bi_2Te_3 . [Adapted from L. Wray *et al.*, *Nature Phys.* **7**, 32 (2011). [22]]

breaking perturbations. Magnetic impurities such as Fe or Mn on the surface of Bi_2Se_3 open a gap at the Dirac point [Figs. 15(a) and 15(b)] [22, 54]. The magnitude of the gap is likely set by the interaction of Fe ions with the Se surface and the time-reversal symmetry breaking disorder potential introduced on the surface. Nonmagnetic disorder created via molecular adsorbent NO_2 or alkali atom adsorption (K or Na) on the surface leaves the Dirac node intact [Figs. 15(c) and 15(d)] in both Bi_2Se_3 and Bi_2Te_3 [17, 55]. These results are consistent with the fact that the topological surface states are protected by time-reversal symmetry.

Many of the interesting theoretical proposals that utilize topological insulator surfaces require the chemical potential to lie at or near the surface Dirac point. This is similar to the case in graphene, where the chemistry of carbon atoms naturally locates the Fermi level at the Dirac point. This makes its density of carriers highly tunable by an applied electrical field and enables applications of graphene to both basic science and microelectronics. The surface Fermi level of a topological insulator depends on the detailed electrostatics of the surface and is not necessarily at the Dirac point. Moreover, for nat-

urally grown Bi_2Se_3 the bulk Fermi energy is not even in the gap. The observed n-type behavior is believed to be caused by Se vacancies. By appropriate chemical modifications, however, the Fermi energy of both the bulk and the surface can be controlled. This allowed [17] to reach the sweet spot in which the surface Fermi energy is tuned to the Dirac point (Fig.16). This was achieved by doping bulk with a small concentration of Ca, which compensates the Se vacancies, to place the Fermi level within the bulk band gap. The surface was the hole doped by exposing the surface to NO_2 gas to place the Fermi level at the Dirac point. These results collectively show how ARPES can be used to study the topological protection and tunability properties of the 2D surface of a 3D topological insulator.

FUTURE DIRECTIONS: IDENTIFYING MAJORANA PLATFORMS AND TOPOLOGICAL SUPERCONDUCTORS

Recent measurements [22] show that surface instabilities cause the spin-helical topological insulator band structure of Bi_2Se_3 to remain well defined and non-degenerate with bulk electronic states at the Fermi level of optimally doped superconducting $\text{Cu}_{0.12}\text{Bi}_2\text{Se}_3$, and that this is also likely to be the case for superconducting variants of p-type Bi_2Te_3 . These surface states provide a highly unusual physical setting in which superconductivity cannot take a conventional form, and is expected to realize one of two novel states that have not been identified elsewhere in nature. If superconducting pairing has even parity, as is nearly universal among the known superconducting materials, the surface electrons will achieve a 2D non-Abelian superconductor state with non-commutative Majorana fermion vortices that can potentially be manipulated to store quantum information. Surface vortices will be found at the end of bulk vortex lines as drawn in Fig.17. If superconducting pairing is odd, the resulting state is a novel state of matter known as a “topological superconductor” with Bogoliubov surface quasi-particles present below the superconducting critical temperature of 3.8 K. As drawn in Fig.17(c), these low temperature surface states would be gapless, likely making it impossible to adiabatically manipulate surface vortices for quantum computation. The unique physics and applications of the topological superconductor state are distinct from any known material system, and will be an exciting vista for theoretical and experimental exploration if they are achieved for the first time in $\text{Cu}_x\text{Bi}_2\text{Se}_3$.

Acknowledgement The authors acknowledge collaborations with A. Bansil, R. J. Cava, J.H. Dil, A. V. Fedorov, Liang Fu, Y. S. Hor, S. Jia, H. Lin, F. Meier, N. P. Ong, J. Osterwalder, L. Patthey, D. Qian and A. Yazdani for collaborations and U.S. DOE Grants No. DE-FG-02-05ER46200, No. AC03-76SF00098, and No. DE-FG02-07ER46352. M.Z.H. acknowledges visiting-scientist sup-

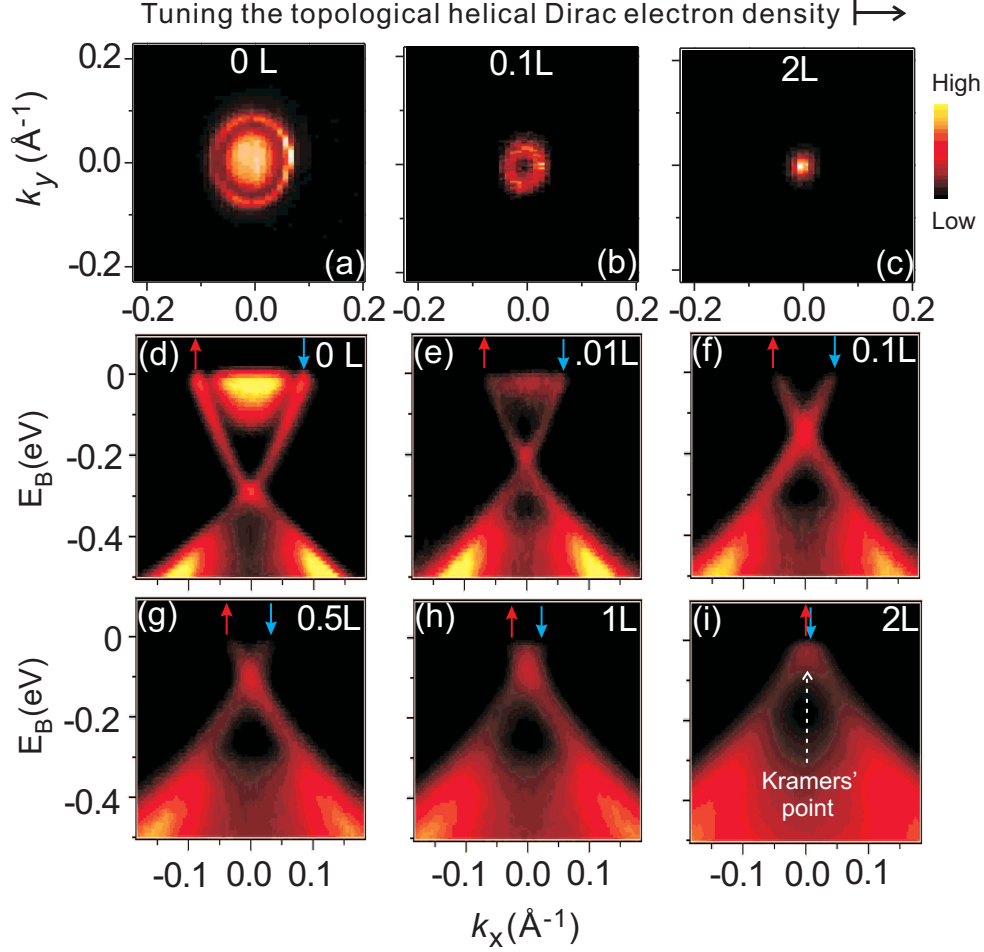


FIG. 16: **Surface Gating : Tuning the density of helical Dirac electrons to the spin-degenerate Kramers point and topological transport regime.** (a) A high resolution ARPES mapping of the surface Fermi surface (FS) near $\bar{\Gamma}$ of $\text{Bi}_{2-\delta}\text{Ca}_\delta\text{Se}_3$ (111). The diffuse intensity within the ring originates from the bulk-surface resonance state [11]. (b) The FS after 0.1 Langmuir (L) of NO_2 is dosed, showing that the resonance state is removed. (c) The FS after a 2 L dosage, which achieves the Dirac charge neutrality point. (d) High resolution ARPES surface band dispersions through after an NO_2 dosage of 0 L, (e) 0.01 L, (f) 0.1 L, (g) 0.5 L, (h) 1 L and (i) 2 L. The arrows denote the spin polarization of the bands. We note that due to an increasing level of surface disorder with NO_2 adsorption, the measured spectra become progressively more diffuse and the total photoemission intensity from the buried $\text{Bi}_{2-\delta}\text{Ca}_\delta\text{Se}_3$ surface is gradually reduced. [Adapted from D. Hsieh *et al.*, *Nature* **460**, 1101 (2009). [17]].

port from Lawrence Berkeley National Laboratory and additional support from the A.P. Sloan Foundation.

SUPPLEMENTARY MATERIALS

Growth method for high-quality single crystals

The undoped and doped $\text{Bi}_{1-x}\text{Sb}_x$ single-crystal samples ($0 \leq x \leq 0.17$) used for ARPES experiments were each cleaved from a boule grown from a stoichiometric mixture of high-purity elements. The boule was cooled from 650 °C to 270 °C over a period of five days and was annealed for seven days at 270 °C. The samples naturally cleaved along the (111) plane, which resulted in shiny flat silver surfaces. X-ray diffraction measurements were used to check that the samples were single phase, and confirmed that the $\text{Bi}_{0.9}\text{Sb}_{0.1}$ single crystals presented

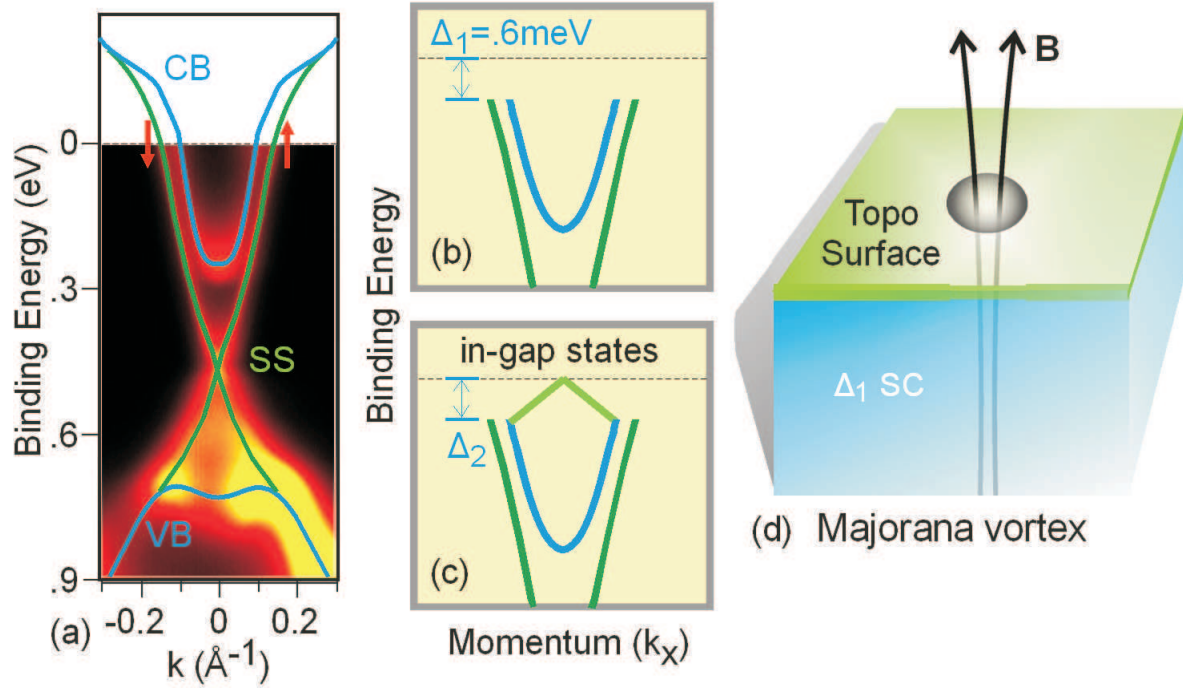


FIG. 17: **A Majorana platform.** (a) Topologically protected surface states cross the Fermi level before merging with the bulk valence and conduction bands in a lightly doped topological insulator. (b) If the superconducting wavefunction has even parity, the surface states will be gapped by the proximity effect, and vortices on the crystal surface will host braidable Majorana fermions. (c) If superconducting parity is odd, the material will be a so-called topological superconductor, and new states will appear below T_c to span the bulk superconducting gap. (d) Majorana fermion surface vortices are found at the end of bulk vortex lines and could be manipulated for quantum computation if superconducting pairing is even. [Adapted from L. Wray *et al.*, *Nature Phys.* **7**, 32 (2011). [22]]

in this paper have a rhombohedral A7 crystal structure (point group $R\bar{3}m$), with room-temperature ($T=300\text{K}$) lattice parameters $a = 4.51 \text{ \AA}$ and $c = 11.78 \text{ \AA}$ indexed using a rhombohedral unit cell. The X-ray diffraction patterns of the cleaved crystals exhibit only the (333), (666), and (999) peaks, showing that the cleaved surface is oriented along the trigonal (111) axis. Room-temperature data were recorded on a Bruker D8 diffractometer using Cu $K\alpha$ radiation ($\lambda = 1.54 \text{ \AA}$) and a diffracted-beam monochromator. The in-plane crystal orientation was determined by Laue X-ray diffraction. During the angle-resolved photoemission spectroscopy (ARPES) measurements a fine alignment was achieved by carefully studying the band dispersions and Fermi surface symmetry as an internal check for crystal orientation.

Resistivity characterization

Temperature-dependent resistivity measurements were carried out on single-crystal samples in a Quantum Design PPMS-9 instrument, using a standard four-probe technique on approximately $4 \times 1 \times 1\text{-mm}^3$, rectangular

samples with the current in the basal plane, which was perpendicular to the trigonal axis. The four contacts were made by using room-temperature silver paste. The data for samples with concentrations ranging from $x = 0$ to $x = 0.17$ showed a systematic change from semimetallic to insulating-like behaviour with increasing x , in agreement with previously published works [27], which was used as a further check of the antimony concentrations. Conventional magnetic and transport measurements [13, 24, 59] such as these cannot separately measure the contributions of the surface and bulk states to the total signal. ARPES, on the other hand, is a momentum-selective technique [41], which allows for a separation of 2D (surface) from 3D (bulk) dispersive energy bands. This capability is especially important for $\text{Bi}_{1-x}\text{Sb}_x$ because the Dirac point lies at a single point in the 3D Brillouin zone, unlike for 2D graphene, where the Dirac points can be studied at any arbitrary perpendicular momentum along a line [39, 60].

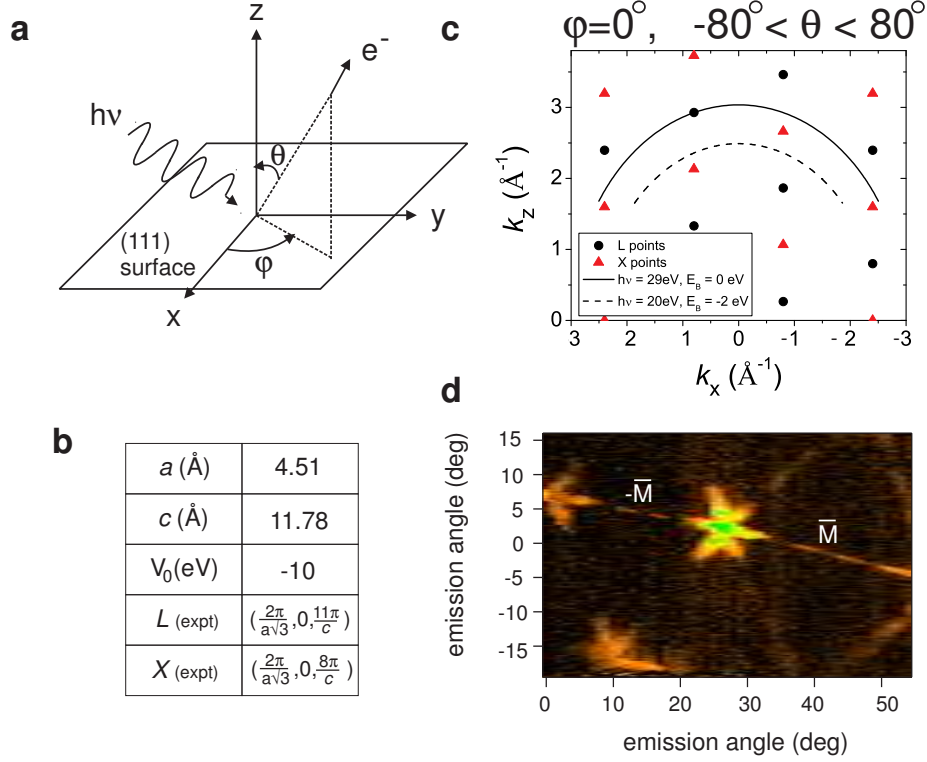


FIG. S1: **Method of locating high symmetry bulk reciprocal lattice points of $\text{Bi}_{0.9}\text{Sb}_{0.1}$ using incident photon energy modulated ARPES.** **a**, Geometry of an ARPES experiment. **b**, Key parameters relevant to the calculation of the positions of the high symmetry points in the 3D BZ. The lattice constants refer to the rhombohedral A7 lattice structure. **c**, Location of L and X points of the bulk BZ in the k_x - k_z plane together with the constant energy contours that can be accessed by changing the angle θ . **d**, Near E_F intensity map ($h\nu = 55$ eV) of the Fermi surface formed by the surface states covering an entire surface BZ, used to help locate various in-plane momenta, in units of the photoelectron emission angle along two orthogonal spatial directions. The electron pockets near \bar{M} in Fig.3c (main text) appear as lines in Fig.S1d due to relaxed k -resolution in order to cover a large k -space in a single shot. [Adapted from D. Hsieh *et al.*, *Nature* **452**, 970 (2008) [14]].

ARPES

Spin-integrated angle-resolved photoemission spectroscopy (ARPES) measurements were performed with 14 to 30 eV photons on beam line 5-4 at the Stanford Synchrotron Radiation Laboratory, and with 28 to 32 eV photons on beam line 12 at the Advanced Light Source, both endstations being equipped with a Scienta hemispherical electron analyzer (see VG Scienta manufacturer website for instrument specifications). Spin-resolved ARPES measurements were performed at the SIS beam line at the Swiss Light Source using the COPHEE spectrometer ([56] p.15) with a single 40 kV classical Mott detector and photon energies of 20 and 22 eV. The typical energy and momentum resolution was 15 meV and 1.5% of the surface Brillouin zone (BZ) respectively at beam line 5-4, 9 meV and 1% of the surface BZ respectively at beam line 12, and 80 meV and 3% of the surface BZ respectively at SIS using a pass energy of 3 eV. Cleaving these samples *in situ* between 10 K and 55 K at chamber pressures less than 5×10^{-11} torr resulted in shiny flat surfaces, characterized *in situ* by low energy

electron diffraction (LEED) to be clean and well ordered with the same symmetry as the bulk. This is consistent with photoelectron diffraction measurements that show no substantial structural relaxation of the Sb(111) surface [57].

Systematic methods for separating bulk from surface electronic states

ARPES is a photon-in, electron-out technique [41]. Photoelectrons ejected from a sample by a monochromatic beam of radiation are collected by a detector capable of measuring its kinetic energy E_{kin} . By varying the detector angles, θ and φ , relative to the sample surface normal, the momentum of the photoelectrons, \mathbf{K} , can also be determined (as illustrated in S1). By employing the commonly used free-electron final state approximation, we can fully convert from the measured kinetic energy and momentum values of the photoelectron to the binding energy, E_B , and Bloch momentum values \mathbf{k} of its initial state inside the crystal, via

Tight binding bandstructure near L point w/ spin-orbit coupling

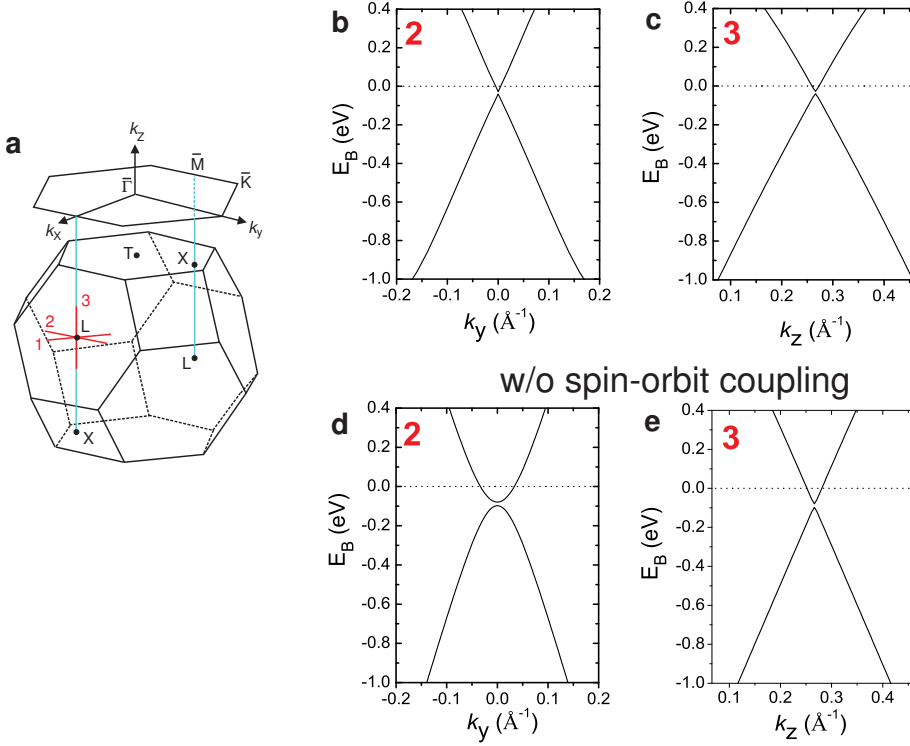


FIG. S2: **Spin-orbit coupling has a profound effect on the band structure of bismuth near L point.** **a**, Schematic of the bulk 3D BZ and the projected BZ of the (111) surface. **b,c**, Calculated tight binding band structure of bismuth including a spin-orbit coupling strength of 1.5 eV along two orthogonal cuts through the L point in the 1st bulk BZ. **d,e**, Tight binding band structure along the same two directions as **b** and **c** calculated without spin-orbit coupling. The inter-band gap of 13.7 meV is barely visible on the scale of **b** and **c**. [Adapted from D. Hsieh *et al.*, *Nature* **452**, 970 (2008) [14]].

$$\begin{aligned}
 |E_B| &= h\nu - W - E_{kin} \\
 k_x &= K_x = \frac{1}{\hbar} \sqrt{2m_e E_{kin}} \sin\theta \\
 k_z &= \frac{1}{\hbar} \sqrt{2m_e (E_{kin} \cos^2\theta - V_0)}
 \end{aligned}$$

where we have set $\varphi = 0$, W is the work function, m_e is the electron mass and V_0 is an experimentally determined parameter, which is approximately -10 eV for bismuth [61, 62]. Features in the ARPES spectra originating from bulk initial states (dispersive along the k_z -direction) were distinguished from those originating from surface initial states (non-dispersive along the k_z -direction) by studying their dependence on incident photon energy, $h\nu$, and converting this to dependence on k_z via the displayed equations. ARPES data were collected at beamlines 12.0.1 and 10.0.1 of the Advanced Light Source at the Lawrence Berkeley National Laboratory, as well as at the PGM beamline of the Synchrotron Radiation Center in Wisconsin, with incident photon energies ranging

from 17 eV to 55 eV, energy resolutions ranging from 9 meV to 40 meV and momentum resolution better than 1.5% of the surface Brillouin zone, using Scienta electron analysers. The combination of high spatial resolution and high crystalline quality enabled us to probe only the highly ordered and cleanest regions of our samples. Single-crystal $\text{Bi}_{1-x}\text{Sb}_x$ samples were cleaved in situ at a temperature of 15 K and chamber pressures less than 8×10^{-11} torr, and high surface quality was checked throughout the measurement process by monitoring the EDC linewidths of the surface state. To measure the near- E_F dispersion of an electronic band along a direction normal to the sample surface, such as the direction from $X(2\pi/\sqrt{3}a, 0, 8\pi/c)$ to $L(2\pi/\sqrt{3}a, 0, 11\pi/c)$ shown in Fig. 3a, EDCs were taken at several incident photon energies. The kinetic energy of the photoelectron at E_F is different for each value of $h\nu$, so the angle was first adjusted and then held fixed for each $h\nu$ so as to keep k_x constant at $2\pi/\sqrt{3}a = 0.8 \text{ \AA}^{-1}$ for electrons emitted near E_F . To ensure that the in-plane momentum remained constant at \bar{M} (the L - X line projects onto \bar{M})

for each EDC, a complete near- E_F intensity map was generated for each photon energy to precisely locate the M-point (see Fig.S1d). We note that because the bulk crystal has only three-fold rotational symmetry about the k_z -axis, the reciprocal lattice does not have mirror symmetry about the $k_x = 0$ plane. Therefore, scans taken at $+\theta$ and $-\theta$ for the same photon energy probe different points in the bulk 3D Brillouin zone; this is responsible for the absence of the bulk Λ -shaped band in Fig. 4f.

Confirming the bulk nature of electronic bands by comparison with theoretical calculations

In an ARPES experiment (Fig.S1a), three dimensional (3D) dispersive bulk electronic states can be identified as those that disperse with incident photon energy, whereas surface states do not. As an additional check that we have indeed correctly identified the bulk bands of $\text{Bi}_{0.9}\text{Sb}_{0.1}$ in Figs 2 and 3, we also measured the dispersion of the deeper lying bands well below the Fermi level (E_F) and compared them to tight binding theoretical calculations of the bulk bands of pure bismuth following the model of Liu and Allen (1995) [25]. A tight-binding approach is known to be valid since $\text{Bi}_{0.9}\text{Sb}_{0.1}$ is not a strongly correlated electron system. As $\text{Bi}_{0.9}\text{Sb}_{0.1}$ is a random alloy (Sb does not form a superlattice [24]) with a relatively small Sb concentration (~ 0.2 Sb atoms per rhombohedral unit cell), the deeper lying band structure of $\text{Bi}_{0.9}\text{Sb}_{0.1}$ is expected to follow that of pure Bi because the deeper lying (localized wave function) bands of $\text{Bi}_{0.9}\text{Sb}_{0.1}$ are not greatly affected by the substitutional disorder, and no additional back folded bands are expected to arise. Since these deeper lying bands are predicted to change dramatically with k_z , they help us to finely determine the experimentally probed k_z values. Fig.S2f shows the ARPES second derivative image (SDI) of a cut parallel to $\bar{K}\bar{M}\bar{K}$ that passes through the L point of the 3D Brillouin zone (BZ), and Fig.S2h shows a parallel cut that passes through the $0.3\ XL$ point (Fig.S2c). The locations of these two cuts in the 3D bulk BZ were calculated from the ARPES kinematic relations, from which we can construct the constant energy contours shown in Fig. S1c. By adjusting θ such that the in-plane momentum k_x is fixed at approximately $0.8\ \text{\AA}^{-1}$ (the surface \bar{M} point), at a photon energy $h\nu = 29\text{ eV}$, electrons at the Fermi energy ($E_B = 0\text{ eV}$) have a k_z that corresponds to the L point in the 3^{rd} bulk BZ. By adjusting θ such that the in-plane momentum k_x is fixed at approximately $-0.8\ \text{\AA}^{-1}$, at a photon energy $h\nu = 20\text{ eV}$, electrons at a binding energy of -2 eV have a k_z near $0.3\ XL$.

There is a clear k_z dependence of the dispersion of measured bands A, B and C, pointing to their bulk nature. The bulk origin of bands A, B and C is confirmed by their good agreement with tight binding calculations (bands 3, 4 and 5 in Figs S2g and i), which include a strong spin-orbit coupling constant of 1.5 eV derived from bismuth

[25]. Band 3 drops below -5 eV at the $0.3\ XL$ point. The slight differences between the experimentally measured band energies and the calculated band energies at $k_y = 0\ \text{\AA}^{-1}$ shown in Fig.S2f-i are due to the fact that the ARPES data were collected in a single shot, taken in constant θ mode. This means that electrons detected at different binding energies will have slightly different values of k_z , whereas the presented tight binding calculations show all bands at a single k_z . We checked that the magnitude of these band energy differences is indeed accounted for by this explanation. Even though the L_a and L_s bands in $\text{Bi}_{0.9}\text{Sb}_{0.1}$ are inverted relative to those of pure semimetallic Bi, calculations show that near E_F , apart from an insulating gap, they are “mirror” bands in terms of k dispersion (see bands 5 and 6 in Fig.S2g). Such a close match to calculations, which also predict a linear dispersion along the k_z cut near E_F (Fig.S2d), provides strong support that the dispersion of band C, near E_F , is in fact linear along k_z . Focusing on the Λ -shaped valence band at L , the EDCs (Fig.S2a) show a single peak out to $k_y \approx \pm 0.15\ \text{\AA}^{-1}$ demonstrating that it is composed of a single band feature. Outside this range however, an additional feature develops on the low binding energy side of the main peak in the EDCs, which shows up as two well separated bands in the SDI image (Fig.3f) and signals a splitting of the band into bulk representative and surface representative components (Fig.S2a,f). Unlike the main peak that disperses strongly with incident photon energy, this shoulder-like feature is present and retains the same Λ -shaped dispersion near this k -region (open circles in Figs S2g and i) for all photon energies used, supporting its 2D surface character. This behaviour is quite unlike bulk band C, which attains the Λ -shaped dispersion only near 29 eV (see main text Fig. 3b).

Spin-orbit coupling is responsible for the unique Dirac-like dispersion behaviour of the bulk bands near E_F

According to theoretical models, a strongly spin-orbit coupled bulk band structure is necessary for topological surface states to exist [10–12, 23?]. Therefore it is important to show that our experimentally measured bulk band structure of $\text{Bi}_{0.9}\text{Sb}_{0.1}$ can only be accounted for by calculations that explicitly include a large spin-orbit coupling term. As shown in the previous section, the measured bulk band dispersion of $\text{Bi}_{0.9}\text{Sb}_{0.1}$ generally follows the calculated bulk bands of pure Bi from a tight binding model. The dispersion of the bulk valence and conduction bands of pure bismuth near E_F at the L point from such a tight binding calculation [25] with a spin-orbit coupling constant of 1.5 eV are shown in Fig. S3b and c, which show a high degree of linearity. The high degree of linearity can be understood from a combination of the large Fermi velocity ($v_F \approx 6\text{ eV}\ \text{\AA}$ along k_y) and small inter-band (below E_F) gap $\Delta = 13.7\text{ meV}$ (Fig. S3). This calculated inter-band gap of

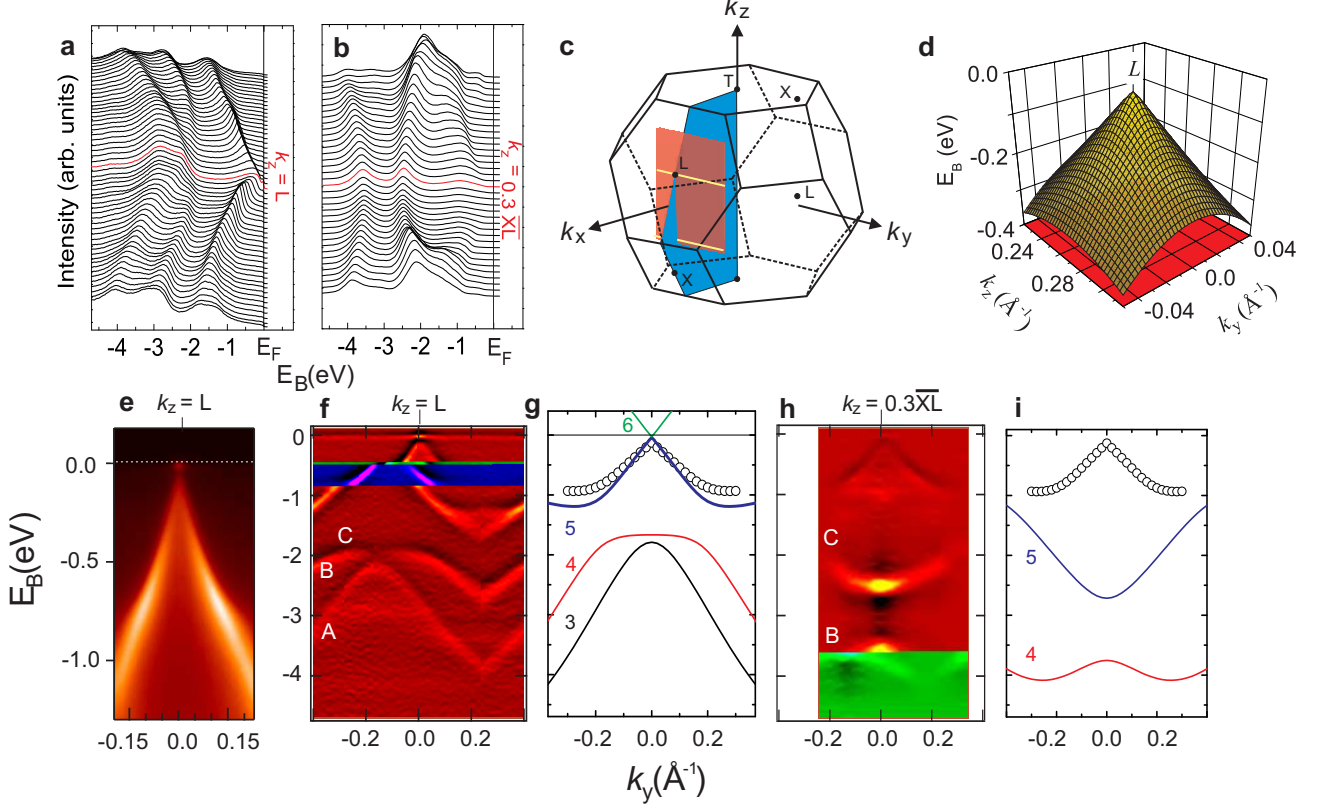


FIG. S3: **Identification of the bulk band features of $\text{Bi}_{0.9}\text{Sb}_{0.1}$.** Experimental band-structure determined by ARPES is compared to bulk tight-binding calculations of bismuth to further identify the deeper lying bulk bands and their symmetry origins. **a**, Energy distribution curves (EDCs) along a k -space cut given by the upper yellow line shown in schematic **c** which goes through the bulk L point in the 3^{rd} BZ ($\hbar\nu = 29$ eV). The corresponding ARPES intensity in the vicinity of L is shown in **e**. **b**, EDCs along the lower yellow line of **c** which goes through the point a fraction 0.3 of the k -distance from X to L ($\hbar\nu = 20$ eV), showing a dramatic change of the deeper lying band dispersions. (This cut was taken at a k_x value equal in magnitude but opposite in sign to that in **a** as described in the SM text). **f, h**, The ARPES second derivative images (SDI) of the raw data shown in **a** and **b** to reveal the band dispersions. The flat band of intensity at E_F is an artifact of taking SDI. **g, i**, Tight binding band calculations of bismuth including spin-orbit coupling, using Liu and Allen model [25], along the corresponding experimental cut directions shown in **f** and **h**. The bands (colored solid lines) labelled 3 to 6 are derived from the symmetries associated with the $6p$ -orbitals and their dispersion is thus strongly influenced by spin-orbit coupling. The inter-band gap between bands 5 and 6 is barely visible on the scale of Fig. S2g. The circled curves mark the surface state dispersion, which is present at all measured photon energies (no k_z dispersion). There is a close match of the bulk band dispersion between the data and calculations, confirming the presence of strong spin-orbit coupling. **d**, Tight binding valence band (5) dispersion of bismuth in the k_y - k_z momentum plane showing linearity along both directions. The close match between data and calculation along k_y suggests that the dispersion near E_F along k_z is also linear. [Adapted from D. Hsieh *et al.*, *Nature* **452**, 970 (2008) [14]].

Bi (13.7 meV) is smaller than our measured lower limit of 50 meV (main text Fig. 2a) for the insulating gap of $\text{Bi}_{0.9}\text{Sb}_{0.1}$. To illustrate the importance of spin-orbit coupling in determining the band structure near L , we show the dispersion along k_y and k_z calculated without spin-orbit coupling (Fig. S3d and e). While the dispersion along k_z is not drastically altered by neglecting the spin-orbit coupling, the dispersion along k_y changes from being linear to highly parabolic. This is further evidence that our measured Dirac point can be accounted for only by including spin-orbit coupling. *A strong spin-orbit cou-*

pling constant acts as an internal quantizing magnetic field for the electron system [32] which can give rise to a quantum spin Hall effect without any externally applied magnetic field [9, 63, 64]. Therefore, the existence or the spontaneous emergence of the surface or boundary states does not require an external magnetic field.

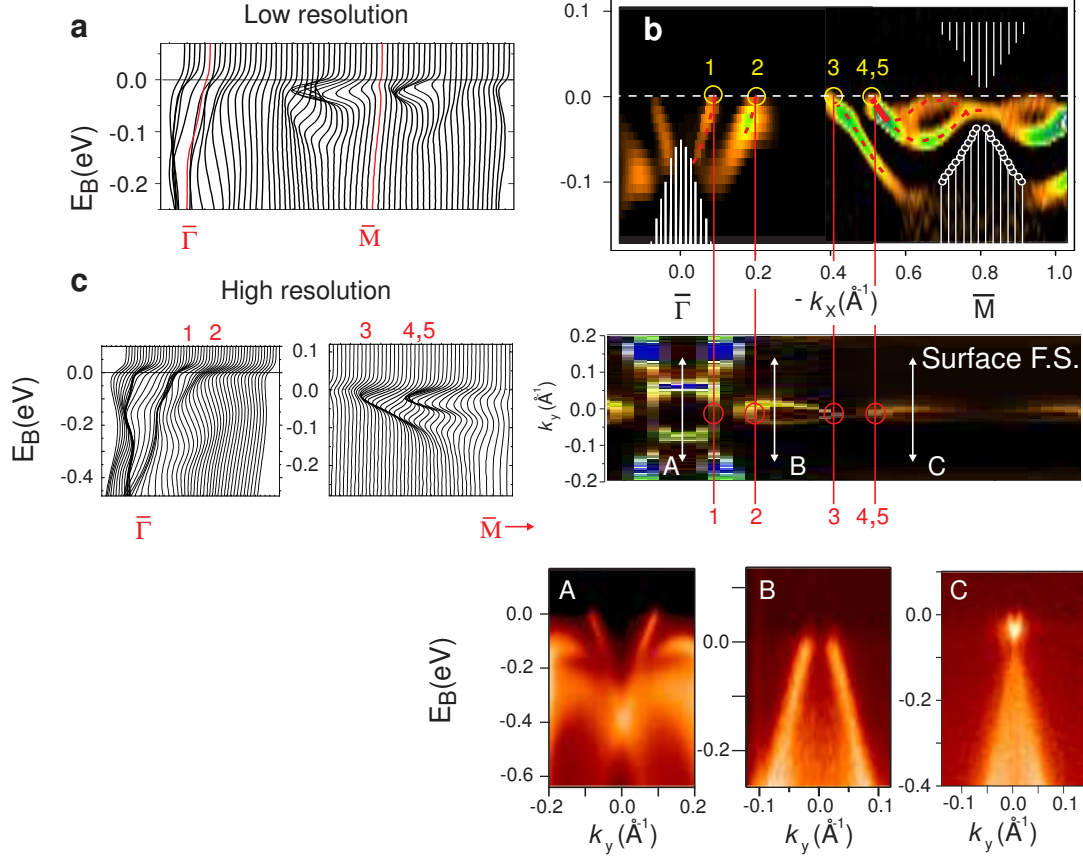


FIG. S4: **The Kramers' point, the gapless nature and topology of surface states in insulating $\text{Bi}_{0.9}\text{Sb}_{0.1}$ is revealed through high spatial and k-resolution ARPES.** **a**, Energy distribution curves (EDCs) of a low resolution ARPES scan along the surface $\bar{\Gamma}$ - \bar{M} cut of $\text{Bi}_{0.9}\text{Sb}_{0.1}$. **b**, The surface band dispersion second derivative image along $\bar{\Gamma}$ - \bar{M} obtained by piecing together four high resolution ARPES scans. See main text Fig.4 for explanation of other features. **c**, EDCs of high resolution ARPES scans in the vicinity of surface Fermi crossings 1 and 2 and crossings 3, 4 and 5 (left panels). These crossings form the surface Fermi surface shown in the upper right panel of **c** (see also main text Fig.3). High resolution ARPES scans along cut directions A, B and C are further evidence for a surface Fermi surface. [Adapted from D. Hsieh *et al.*, *Nature* **452**, 970 (2008) [14]].

Matching the surface state Fermi crossings and the topology of the surface Fermi surface in bulk insulating $\text{Bi}_{0.9}\text{Sb}_{0.1}$

In order to count the number of singly degenerate surface state Fermi crossings [8, 42, 65] along the $\bar{\Gamma}$ - \bar{M} cut of the surface BZ, high photon energy ARPES scans, which allow mapping of the entire k range from $\bar{\Gamma}$ - \bar{M} to fall within the detector window at the expense of lower instrument resolution, were taken to preliminarily identify the k-space locations of the Fermi crossings (Fig. S4a). Having determined where these surface state Fermi crossings lie in k-space, we performed several high resolution ARPES scans, each covering a successive small k interval in the detector window, in order to construct a high resolution band mapping of the surface states from $\bar{\Gamma}$ to \bar{M} . The second derivative image of the surface band dispersion shown in Fig.S4b was constructed by piecing

together four such high resolution scans. Fig.S4c shows energy distribution curves of high resolution ARPES scans in the vicinity of each surface Fermi crossing, which together give rise to the surface Fermi surface shown. No previous work [8, 34–38] has reported the band dispersion near the L -point (thus missing the Dirac bands) or resolved the Kramers point near the \bar{M} point, which is crucial to determine the topology of the surface states. For this reason there is no basis for one-to-one comparison with previous work, since no previous ARPES data exists in the analogous k-range. Note that surface band dispersions along the cuts A, B and C are highly linear. This is indirect evidence for the existence of the bulk Dirac point since surface states are formed when the bulk state wave functions are subjected to the boundary conditions at the cleaved plane.

Two-step fitting analysis procedure of Spin-Resolved ARPES measurements of insulating $\text{Bi}_{1-x}\text{Sb}_x$

Here we present details of the spin-resolved ARPES analysis on bulk insulating $\text{Bi}_{0.91}\text{Sb}_{0.09}$ that show how we arrive at a spin-resolved surface band dispersion such as that presented in Figure 5(G) in the main text. In the VUV incident photon energy regime that we use, spin conserving photoemission processes (where the electric field of light only acts on the orbital degree of freedom of the electron inside a solid) dominate over spin non-conserving processes (which arise from coupling to the magnetic field of light) [58]. Therefore we are confident that the photo-emission process does not change the spin polarization of the electrons. Figure S5(B) shows a spin averaged momentum distribution curve (MDC) along the $\bar{\Gamma}$ to -M direction taken at $E_B = -25$ meV, indicated by the green line shown in Figure S5(A). This MDC was obtained by summing the signal coming from both left and right electron detectors in the Mott polarimeter (see diagram in Fig.9(A) of the main text). Lorentzian line-shapes denoted I^i and a non-polarized background B are fitted to this MDC, which are used as inputs to the two-step fitting routine developed by Meier *et al.* [45] in the following way. To begin with, a spin polarization vector $\vec{P}_M^i = (P_{x'}^i, P_{y'}^i, P_{z'}^i) = (\cos \theta_i \cos \phi_i, \cos \theta_i \sin \phi_i, \sin \theta_i)$ is assigned to each band, where θ_i and ϕ_i are referenced to the primed Mott coordinate frame. Here it is necessary to assume a spin magnitude of one because only two spin components are measured by a single Mott detector. Such an assumption is likely valid since even though the spin polarization is no longer a good quantum number due to spin-orbit coupling, the bands near $\bar{\Gamma}$ are expected to exhibit a high degree of spin polarization since the spin-orbit coupling is smallest near $\bar{\Gamma}$. Moreover, common strong spin-orbit coupled materials such as gold have been experimentally shown to exhibit 100% spin polarized surface states [46]. A spin-resolved spectrum is then defined for each peak i using $I_\alpha^{i;\uparrow,\downarrow} = I^i(1 \pm P_\alpha^i)/6$, where $\alpha = x', y', z'$, and $+$ and $-$ correspond to the spin direction being parallel (\uparrow) or antiparallel (\downarrow) to α . The full spin-resolved spectrum is then given by $I_\alpha^{\uparrow,\downarrow} = \sum_i I_\alpha^{i;\uparrow,\downarrow} + B/6$, where B is the unpolarized background, from which the spin polarization of each spatial component can be obtained as $P_\alpha = (I_\alpha^\uparrow - I_\alpha^\downarrow)/(I_\alpha^\uparrow + I_\alpha^\downarrow)$. This latter expression is a function of θ_i and ϕ_i and is used to fit to the experimental data.

The spin polarization data for the y' and z' components (i.e. $P_{y'}$ and $P_{z'}$) are obtained by taking the difference between the intensities of the left-right (or top-bottom) electron detectors over their sum, all divided by the Sherman function, which is calibrated using the methods in ([56], p.36). Typical electron counts on the detector reach 5×10^5 , which places an error bar of approximately ± 0.01 for each point on our polarization curves. To account for unequal sensitivities between a detector pair, we applied a small multiplicative factor to the intensity from one detector to ensure that the unpo-

larized background intensity yields zero polarization. Resultant curves are shown in Figure S5(C). The best fit parameters $(P_{x'}^i, P_{y'}^i, P_{z'}^i)$, which are expressed in the sample coordinates through an appropriate coordinate transformation [inset of Fig. S5(C)] are shown in Figure S5(D). Even though the measured polarization only reaches a magnitude of around ± 0.1 , this is similarly seen in studies of Bi thin films [42] and is due to the non-polarized background and overlap of adjacent peaks with different spin polarization. These effects are extremely sensitive to the sample alignment due to the very narrow Fermi surface features. The fitted parameters [Fig. S5(D)] are consistent with spins being nearly aligned along the $\pm \hat{y}$ direction, with bands $l1$ and $r1$ having nearly opposite spin as required by time reversal symmetry, and with these spins nearly parallel to those of $l1$ and $r1$ respectively measured for Sb [main text Fig.9(F)]. The small departures from ideality likely originate from the scan direction not being exactly along $\bar{\Gamma}$ - \bar{M} . Bands $l1$ and $l2$ display opposite spin, which indicates that they form a Kramers pair split by spin-orbit coupling, and the fact that bands $l2$ and $l3$ have the same spin suggests that they originate from the same band.

To show that bands $l2$ and $l3$ connect above E_F as we have drawn in Figure S5(A), and are thus expected to have the same spin, we map the surface band dispersion of Te doped $\text{Bi}_{1-x}\text{Sb}_x$ that is known to be an electron donor [66]. Figure S5(F) shows that the hole band formed by crossings 2 and 3 in insulating $\text{Bi}_{1-x}\text{Sb}_x$ [Fig. S5(A)] has sunk completely below E_F with 0.5% Te doping, and is in fact the same band.

Method of using incident photon energy modulated ARPES to separate the bulk from surface electronic states of Sb

In this section we detail incident photon energy modulated ARPES experiments on the low lying electronic states of single crystal Sb(111), which we employ to isolate the surface from bulk-like electronic bands over the entire BZ. Figure S6(C) shows momentum distributions curves (MDCs) of electrons emitted at E_F as a function of k_x ($\parallel \bar{\Gamma}$ - \bar{M}) for Sb(111). The out-of-plane component of the momentum k_z was calculated for different incident photon energies ($h\nu$) using the free electron final state approximation with an experimentally determined inner potential of 14.5 eV [68, 69]. There are four peaks in the MDCs centered about $\bar{\Gamma}$ that show no dispersion along k_z and have narrow widths of $\Delta k_x \approx 0.03 \text{ \AA}^{-1}$. These are attributed to surface states and are similar to those that appear in Sb(111) thin films [68]. As $h\nu$ is increased beyond 20 eV, a broad peak appears at $k_x \approx -0.2 \text{ \AA}^{-1}$, outside the k range of the surface states near $\bar{\Gamma}$, and eventually splits into two peaks. Such a strong k_z dispersion, together with a broadened linewidth ($\Delta k_x \approx 0.12 \text{ \AA}^{-1}$), is indicative of bulk band behavior, and indeed these MDC peaks trace out a Fermi surface [Fig. S6(D)]

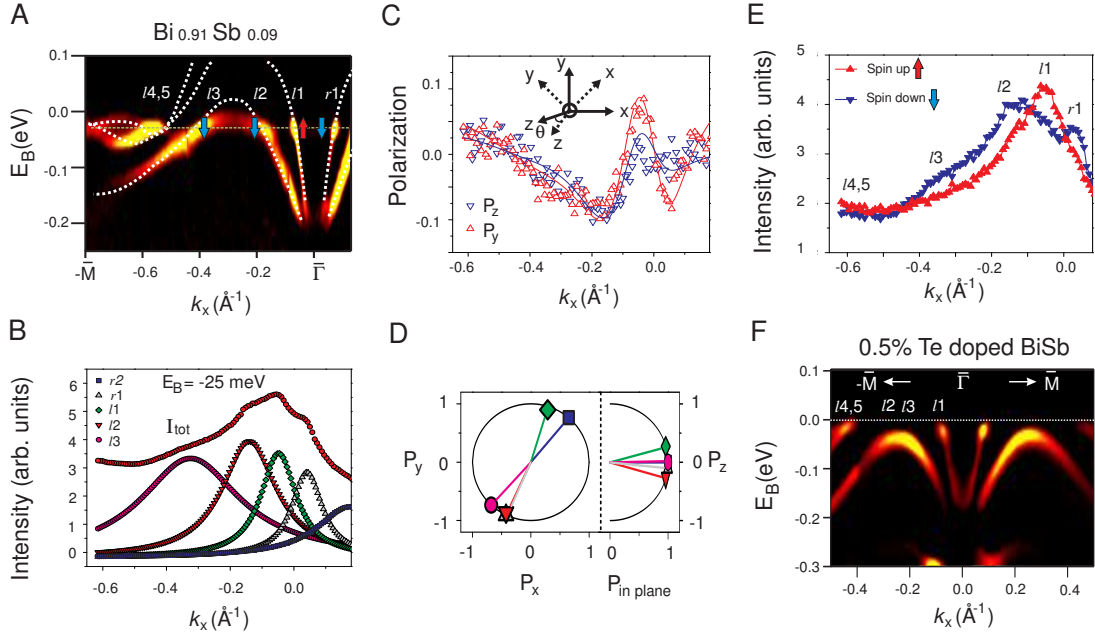


FIG. S5: (A) The surface band dispersion ARPES second derivative image (SDI) along the $\bar{\Gamma}$ to \bar{M} direction of bulk insulating Bi_{0.91}Sb_{0.09}. Dashed white lines are guides to the eye. The intensity of bands $l/4,5$ is scaled up for clarity. (B) MDC of the spin averaged spectrum at $E_B = -25$ meV [green line below E_F in (A)] using a photon energy $h\nu = 22$ eV, together with the Lorentzian peaks of the fit. (C) Measured spin polarization curves (symbols) for the y' and z' (Mott coordinate) components together with the fitted lines (SM). The relative orientation of the sample (un-primed) to Mott (primed) coordinates is shown in the inset. The polar angle θ is rotated during the measurement to access different values of k_x . At normal emission ($\theta = 0^\circ$), the z' and z axes are parallel and the y' axis is rotated from the y axis by 45° . (D) The in-plane and out-of-plane spin polarization components in the sample coordinate frame obtained from the spin polarization fit. The symbols refer to those in (B). The fitted parameters are consistent with 100% polarized spins. (E) Spin resolved spectra for the y component based on the fitted spin polarization curves shown in (C). Spin up (down) refers to the spin direction being approximately parallel to the $+\hat{y}$ ($-\hat{y}$) direction. (F) The surface band dispersion SDI centered about $\bar{\Gamma}$ of (Bi_{0.925}Sb_{0.075})_{0.995}Te_{0.005}. Electron doping through Te reveals that bands $l/2$ and $l/3$ are connected above E_F . [Adapted from D. Hsieh *et al.*, *Science* **323**, 919 (2009) [16]].

that is similar in shape to the hole pocket calculated for bulk Sb near H [67]. Therefore by choosing an appropriate photon energy (e.g. ≤ 20 eV), the ARPES spectrum at E_F along $\bar{\Gamma}$ - \bar{M} will have contributions from only the surface states. The small bulk electron pocket centered at L is not accessed using the photon energy range we employed [Fig. S6(D)].

Now we describe the experimental procedure used to distinguish pure surface states from resonant states on Sb(111) through their spectral signatures. ARPES spectra along $\bar{\Gamma}$ - \bar{M} taken at three different photon energies are shown in Fig. S7. Near $\bar{\Gamma}$ there are two rather linearly dispersive electron like bands that meet exactly at $\bar{\Gamma}$ at a binding energy $E_B \sim -0.2$ eV. This behavior is consistent with a pair of spin-split surface bands that become degenerate at the time reversal invariant momentum (\vec{k}_T) $\bar{\Gamma}$ due to Kramers degeneracy. The surface origin of this pair of bands is established by their lack of dependence on $h\nu$ [Fig. S7(A)-(C)]. A strongly photon energy dispersive hole like band is clearly seen on the negative k_x side of the surface Kramers pair, which crosses E_F for $h\nu = 24$ eV and gives rise to the bulk hole Fermi surface near H [Fig. S6(D)]. For $h\nu \leq 20$ eV, this band shows clear

back folding near $E_B \approx -0.2$ eV indicating that it has completely sunk below E_F . Further evidence for its bulk origin comes from its close match to band calculations [Fig. S6(D)]. Interestingly, at photon energies such as 18 eV where the bulk bands are far below E_F , there remains a uniform envelope of weak spectral intensity near E_F in the shape of the bulk hole pocket seen with $h\nu = 24$ eV photons, which is symmetric about $\bar{\Gamma}$. This envelope does not change shape with $h\nu$ suggesting that it is of surface origin. Due to its weak intensity relative to states at higher binding energy, these features cannot be easily seen in the energy distribution curves (EDCs) in Fig. S7(A)-(C), but can be clearly observed in the MDCs shown in Fig. S6(C) especially on the positive k_x side. Centered about the \bar{M} point, we also observe a crescent shaped envelope of weak intensity that does not disperse with k_z [Fig. S7(D)-(F)], pointing to its surface origin. Unlike the sharp surface states near $\bar{\Gamma}$, the peaks in the EDCs of the feature near \bar{M} are much broader ($\Delta E \sim 80$ meV) than the spectrometer resolution (15 meV). The origin of this diffuse ARPES signal is not due to surface structural disorder because if that were the case, electrons at $\bar{\Gamma}$ should be even more severely scattered

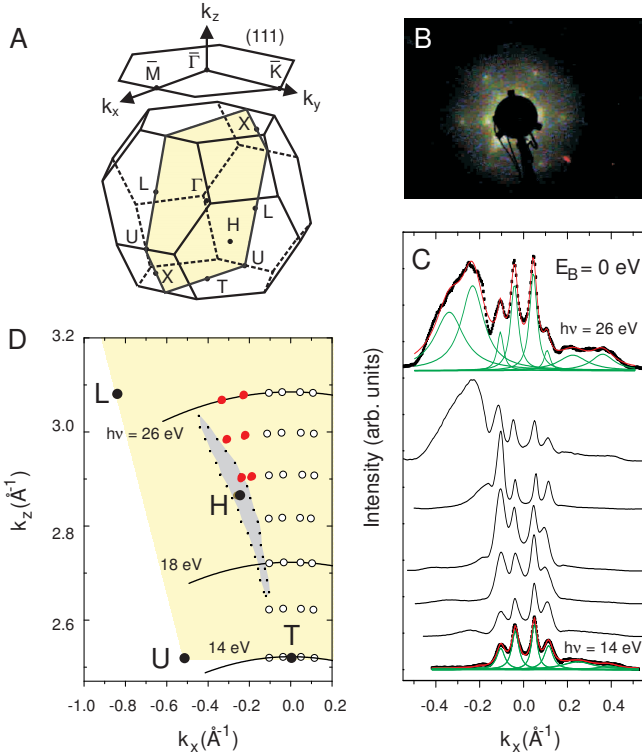


FIG. S6: (A) Schematic of the bulk BZ of Sb and its (111) surface BZ. The shaded region denotes the momentum plane in which the following ARPES spectra were measured. (B) LEED image of the *in situ* cleaved (111) surface exhibiting a hexagonal symmetry. (C) Select MDCs at E_F taken with photon energies from 14 eV to 26 eV in steps of 2 eV, taken in the *TXLU* momentum plane. Peak positions in the MDCs were determined by fitting to Lorentzians (green curves). (D) Experimental 3D bulk Fermi surface near H (red circles) and 2D surface Fermi surface near $\bar{\Gamma}$ (open circles) projected onto the k_x - k_z plane, constructed from the peak positions found in (C). The k_z values are determined using calculated constant $h\nu$ contours (black curves) (SM). The shaded gray region is the theoretical hole Fermi surface calculated in [67]. [Adapted from D. Hsieh *et al.*, *Science* **323**, 919 (2009) [16]].

from defects than those at \bar{M} . In fact, the occurrence of both sharp and diffuse surface states originates from a k dependent coupling to the bulk. As seen in Fig. 7(D) of the main text, the spin-split Kramers pair near $\bar{\Gamma}$ lie completely within the gap of the projected bulk bands near E_F attesting to their purely surface character. In contrast, the weak diffuse hole like band centered near $k_x = 0.3 \text{ \AA}^{-1}$ and electron like band centered near $k_x = 0.8 \text{ \AA}^{-1}$ lie completely within the projected bulk valence and conduction bands respectively, and thus their ARPES spectra exhibit the expected lifetime broadening due to coupling with the underlying bulk continuum [70].

Method of counting spin Fermi surface \vec{k}_T enclosures in pure Sb

In this section we give a detailed explanation of why the surface Fermi contours of Sb(111) that overlap with the projected bulk Fermi surfaces can be neglected when determining the ν_0 class of the material. Although the Fermi surface formed by the surface resonance near \bar{M} encloses the $\vec{k}_T \bar{M}$, we will show that this Fermi surface will only contribute an even number of enclosures and thus not alter the overall evenness or oddness of \vec{k}_T enclosures. Consider some time reversal symmetric perturbation that lifts the bulk conduction L_a band completely above E_F so that there is a direct excitation gap at L. Since this perturbation preserves the energy ordering of the L_a and L_s states, it does not change the ν_0 class. At the same time, the weakly surface bound electrons at \bar{M} can evolve in one of two ways. In one case, this surface band can also be pushed up in energy by the perturbation such that it remains completely inside the projected bulk conduction band [Fig. S8(A)]. In this case there is no more density of states at E_F around \bar{M} . Alternatively the surface band can remain below E_F so as to form a pure surface state residing in the projected bulk gap. However by Kramers theorem, this SS must be doubly spin degenerate at \bar{M} and its FS must therefore enclose \bar{M} twice [Fig. S8(B)]. In determining ν_0 for semi-metallic Sb(111), one can therefore neglect all segments of the FS that lie within the projected areas of the bulk FS [Fig. 7(G) of main text] because they can only contribute an even number of FS enclosures, which does not change the modulo 2 sum of \vec{k}_T enclosures.

In order to further experimentally confirm the topologically non-trivial surface band dispersion shown in figures 7(C) and (D) of the main text, we show ARPES intensity maps of Sb(111) along the $-\bar{K}-\bar{\Gamma}-\bar{K}$ direction. Figure S8(C) shows that the inner V-shaped band that was observed along the $-\bar{M}-\bar{\Gamma}-\bar{M}$ direction retains its V-shape along the $-\bar{K}-\bar{\Gamma}-\bar{K}$ direction and continues to cross the Fermi level, which is expected since it forms the central hexagonal Fermi surface. On the other hand, the outer V-shaped band that was observed along the $-\bar{M}-\bar{\Gamma}-\bar{M}$ direction no longer crosses the Fermi level along the $-\bar{K}-\bar{\Gamma}-\bar{K}$ direction, instead folding back below the Fermi level around $k_y = 0.1 \text{ \AA}^{-1}$ and merging with the bulk valence band [Fig. S8(C)]. This confirms that it is the $\Sigma_{1(2)}$ band starting from $\bar{\Gamma}$ that connects to the bulk valence (conduction) band, in agreement with the calculations shown in figure 7(D) of the main text.

Physical interpretation of n_M : the mirror Chern number and an analogy with the spin-Chern number

In this section we will describe how a mirror Chern number arises from the crystal symmetry of $\text{Bi}_{1-x}\text{Sb}_x$. Electronic states in the mirror plane ($k_y = 0$) [Fig. S9(A)] are eigenstates of the mirror operator $M(\hat{y})$ with eigen-

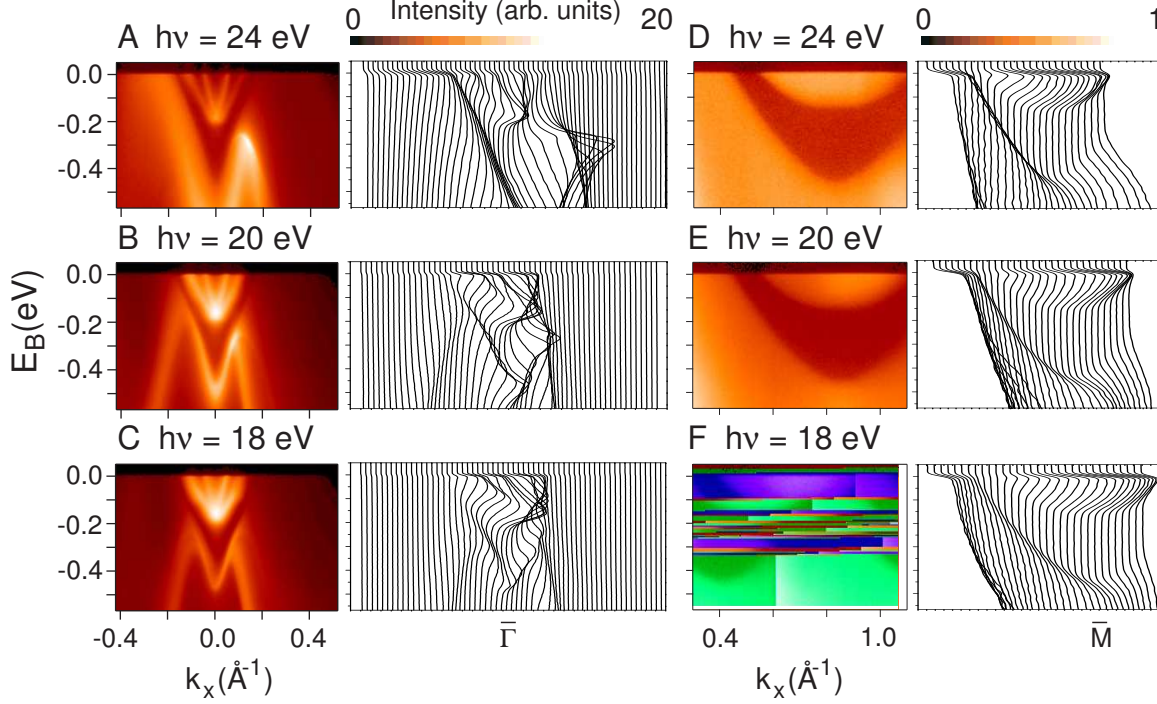


FIG. S7: ARPES intensity maps of Sb(111) as a function of k_x near $\bar{\Gamma}$ (A)-(C) and \bar{M} (D)-(F) and their corresponding energy distribution curves, taken using $h\nu = 24$ eV, 20 eV and 18 eV photons. The intensity scale of (D)-(F) is a factor of about twenty smaller than that of (A)-(C) due to the intrinsic weakness of the ARPES signal near \bar{M} . [Adapted from D. Hsieh *et al.*, *Science* **323**, 919 (2009) [16]].

values $\pm i$. $M(\hat{y})$ is closely related to, but not exactly the same as the spin operator S_y . It may be written as $M(\hat{y}) = PC_2(\hat{y})$: the product of the parity operator $P : (x, y, z) \rightarrow (-x, -y, -z)$ and a twofold rotation operator $C_2(\hat{y}) : (x, y, z) \rightarrow (-x, y, -z)$. For a free spin, P does not affect the pseudovector spin, and $C_2(\hat{y})$ simply rotates the spin. Thus, $M(\hat{y}) = \exp[-i\pi S_y/\hbar]$. For spin eigenstates $S_y = \pm\hbar/2$, this gives $M(\hat{y}) = \mp i$. In the crystal with spin-orbit interaction on the other hand, S_y is no longer a good quantum number, but $M(\hat{y})$ still is. The energy bands near the Fermi energy in $\text{Bi}_{1-x}\text{Sb}_x$ are derived from states with even orbital mirror symmetry and satisfy $M(\hat{y}) \propto -i \text{sign}(\langle S_y \rangle)$, as detailed in [40] and summarized below.

Unlike the bulk states which are doubly spin degenerate, the surface state spin degeneracy is lifted due to the loss of crystal inversion symmetry at the surface, giving rise to the typical Dirac like dispersion relations near time reversal invariant momenta [Fig. S9(B)&(C)]. For surface states in the mirror plane $k_y = 0$ with $M(\hat{y}) = \pm i$, the spin split dispersion near $k_x = 0$ has the form $E = \pm\hbar v k_x$. Assuming no other band crossings occur, the sign of the velocity v is determined by the topological mirror Chern number (n_M) describing the bulk band structure. When $n_M = 1$, the situation in figure S9(B)

is realized where it is the spin up ($\langle S_y \rangle \parallel \hat{y}$) band that connects the bulk valence to conduction band going in the positive k_x direction (i.e. the spin up band has a velocity in the positive x direction). For $n_M = -1$ the opposite holds true [Fig. S9(C)]. These two possibilities also lead to two distinct chiralities of the central Fermi surface as shown in figures S9(B)&(C). From our spin-resolved ARPES data on both insulating $\text{Bi}_{1-x}\text{Sb}_x$ and pure Sb, we find that the surface polarized band dispersions are consistent with $n_M = -1$ [Figs S9(D)&(E)], suggesting that their bulk electron wavefunctions exhibit the anomalous value $n_M = -1$ predicted in (42), which is not realizable in free electron systems with full rotational symmetry.

There is an intimate physical connection between a 2D quantum spin Hall insulator and the 2D k -space mirror plane of a 3D topological insulator. In the former case, the occupied energy bands for each spin eigenvalue will be associated with an ordinary Chern integer $n_{\uparrow,\downarrow}$, from which a non-zero spin-Chern number can be defined $n_s = (n_{\uparrow} - n_{\downarrow})/2$. In the latter case, it is the mirror eigenvalue of the occupied energy bands that have associated with them Chern integers $n_{+i,-i}$, from which a non-zero mirror Chern number can be defined $n_M = (n_{+i} - n_{-i})/2$.

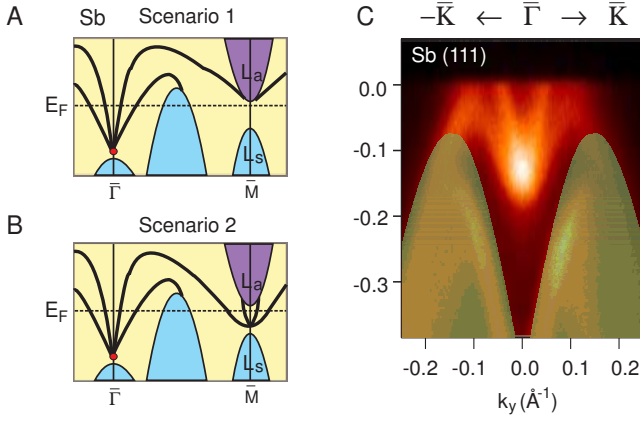


FIG. S8: (A) Schematic of the surface band structure of Sb(111) under a time reversal symmetric perturbation that lifts the bulk conduction (L_a) band above the Fermi level (E_F). Here the surface bands near \bar{M} are also lifted completely above E_F . (B) Alternatively the surface band near \bar{M} can remain below E_F in which case it must be doubly spin degenerate at \bar{M} . (C) ARPES intensity plot of the surface states along the $-\bar{K}-\bar{\Gamma}-\bar{K}$ direction. The shaded green regions denote the theoretical projection of the bulk valence bands, calculated using the full potential linearized augmented plane wave method using the local density approximation including the spin-orbit interaction (method described in 40). Along this direction, it is clear that the outer V-shaped surface band that was observed along the $-\bar{M}-\bar{\Gamma}-\bar{M}$ now merges with the bulk valence band. [Adapted from D. Hsieh *et al.*, *Science* **323**, 919 (2009) [16]].

-
- [1] N. W. Ashcroft & N. D. Mermin, *Solid State Physics* (Holt, Rinehart and Winston, New York, 1976).
- [2] K. v. Klitzing, G. Dorda & M. Pepper, *Phys. Rev. Lett.* **45**, 494 (1980).
- [3] D. C. Tsui, H. L. Stormer, & A. C. Gossard, *Phys. Rev. Lett.* **48**, 1559 (1982).
- [4] R. B. Laughlin, *Phys. Rev. Lett.* **50**, 1395 (1983).
- [5] X.-G. Wen, *Int. J. Mod. Phys. B* **4**, 239 (1990).
- [6] D. J. Thouless *et al.*, *Phys. Rev. Lett.* **49**, 405 (1982).
- [7] J. E. Avron, D. Osadchy & R. Seiler, *Phys. Today* **56** (8), 38 (2003).
- [8] C. L. Kane & E. J. Mele, *Phys. Rev. Lett.* **95**, 146802 (2005).
- [9] B. A. Bernevig, T. L. Hughes & S.-C. Zhang, *Science* **314**, 1757 (2006).
- [10] L. Fu & C. L. Kane, *Phys. Rev. B* **76**, 045302 (2007).
- [11] J. E. Moore & L. Balents, *Phys. Rev. B* **75**, 121306(R) (2007).
- [12] L. Fu, C. L. Kane & E. J. Mele, *Phys. Rev. Lett.* **98**, 106803 (2007).
- [13] M. König *et al.*, *Science* **318**, 766 (2007).
- [14] D. Hsieh *et al.*, *Nature* **452**, 970 (2008) [Completed and submitted in **2007**]. Also see KITP Proceeding at <http://online.itp.ucsb.edu/online/motmaterials07/hasan/> (**2007**).
- [15] Y. Xia *et al.*, *Nature Phys.* **5**, 398 (2009). [Completed and submitted in **2008**]. Preprint at <http://aps.arxiv.org/abs/0812.2078> (2008).
- [16] D. Hsieh *et al.*, *Science* **323**, 919 (2009). [Completed and submitted in **2008**].
- [17] D. Hsieh *et al.*, *Nature* **460**, 1101 (2009).
- [18] Y.L. Chen *et al.*, *Science* **325**, 178 (2009).
- [19] H. Zhang *et al.*, *Nature Phys.* **5**, 438 (2009).
- [20] D. Hsieh *et al.*, *Phys. Rev. Lett.* **103**, 146401 (2009).
- [21] L.A. Wray *et al.*, *Nature Phys.* **6**, 855 (2010).
- [22] L.A. Wray *et al.*, *Nature Phys.* **7**, 32 (2011).
- [23] S. Murakami, *New. J. Phys.* **9**, 356 (2007).
- [24] B. Lenoir *et al.* Bi-Sb alloys: an update. *Fifteenth International Conference on Thermoelectrics*, 1-13 (1996).
- [25] Y. Liu & E. Allen, *Phys. Rev.* **B52**, 1566 (1995).
- [26] P. A. Wolff, *J. Phys. Chem. Solids* **25**, 1057 (1964).
- [27] H. Fukuyama & R. Kubo, *J. Phys. Soc. Jpn.* **28**, 570 (1970).
- [28] F. A. Buot, *Phys. Rev.* **A8**, 1570 (1973).
- [29] L. C. Hebel & G. E. Smith, *Phys. Lett.* **10**, 273 (1964).
- [30] Y. Zhang *et al.*, *Nature* **438**, 201 (2005).
- [31] S. Y. Zhou *et al.*, *Nature Mat.* **6**, 770 (2007).
- [32] F. D. M. Haldane, *Phys. Rev. Lett.* **61**, 2015 (1988).
- [33] C. R. Ast & H. Hochst, *Phys. Rev. Lett.* **87**, 177602 (2001).
- [34] H. Hochst & S. Gorovikov, *J. Elect. Spectrosc. Relat. Phenom.* **351**, 144 (2005). This work does not measure

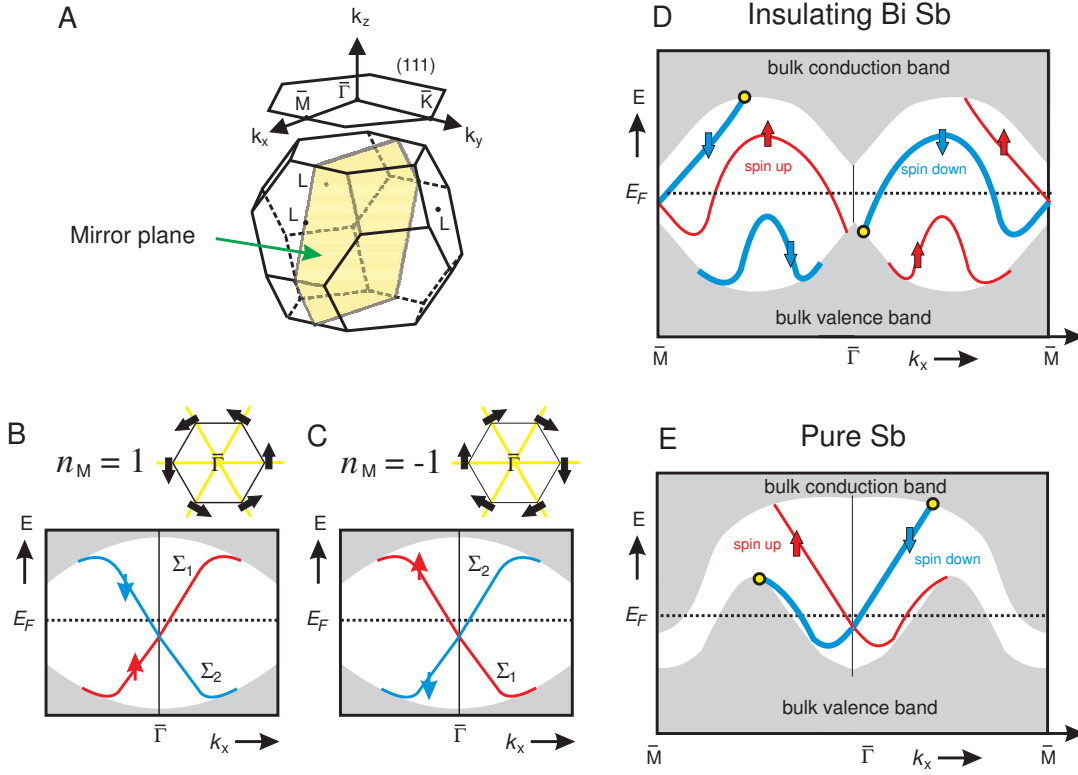


FIG. S9: **Measurement of topological mirror Chern number: The k -space mirror symmetry and the topological spin states on the surface.** (A) 3D bulk Brillouin zone and the mirror plane in reciprocal space. (B) Schematic spin polarized surface state band structure for a mirror Chern number (n_M) of +1 and (C) -1. Spin up and down mean parallel and anti-parallel to \hat{y} respectively. The upper (lower) shaded gray region corresponds to the projected bulk conduction (valence) band. The hexagons are schematic spin polarized surface Fermi surfaces for different n_M , with yellow lines denoting the mirror planes. (D) Schematic representation of surface state band structure of insulating $\text{Bi}_{1-x}\text{Sb}_x$ and (E) semi metallic Sb both showing a $n_M = -1$ topology. Yellow circles indicate where the spin down band (bold) connects the bulk valence and conduction bands. [Adapted from D. Hsieh *et al.*, *Science* **323**, 919 (2009) [16]].

- the surface state along the critical $\bar{\Gamma} - \bar{M}$ direction or detect the bulk Dirac spectrum near L.
- [35] P. Hofmann, *Prog. Surf. Sci.* **81**, 191 (2006).
 - [36] T. Hirahara *et al.*, *Phys. Rev.* **B76**, 153305 (2007).
 - [37] M. Hengsberger *et al.* *Eur. Phys. J.* **17**, 603 (2000).
 - [38] C. R. Ast & H. Hochst, *Phys. Rev.* **B67**, 113102 (2003).
 - [39] K. S. Novoselov *et al.*, *Science* **315**, 1379 (2007).
 - [40] J. C. Y. Teo, L. Fu & C. L. Kane, *Phys. Rev. B* **78**, 045426 (2008).
 - [41] S. Hufner, *Photoelectron Spectroscopy* (Springer-. verlag, Berlin, 1995).
 - [42] T. Hirahara *et al.*, *Phys. Rev. B* **76**, 153305 (2007).
 - [43] J. J. Sakurai, *Modern Quantum Mechanics* (Addison-Wesley, New York, 1994).
 - [44] X. -L. Qi, T. Hughes & S. -C. Zhang, *Phys. Rev. B* **78**, 195424 (2008).
 - [45] F. Meier *et al.*, *Phys. Rev. B* **77**, 165431 (2008).
 - [46] M. Hoesch *et al.*, *Phys. Rev. B* **69**, 241401(R) (2004).
 - [47] K. Sugawara *et al.*, *Phys. Rev. Lett.* **96**, 046411 (2006).
 - [48] M. Hoesch *et al.*, *J. Electron Spectrosc. Relat. Phenom.* **124**, 263 (2002).
 - [49] T. J. Gay & F. B. Dunning, *Rev. Sci. Instrum.* **63**, 1635 (1992).
 - [50] S.-Y. Xu *et al.*, *Science* **332** 560 (2011).
 - [51] L. Fu & C. L. Kane, *Phys. Rev. Lett.* **100**, 096407 (2008).
 - [52] P. J. Leek *et al.*, *Science* **318**, 1889 (2007).
 - [53] A. Kitaev, *Ann. Phys. (NY)* **303**, 2 (2003).
 - [54] Y. S. Hor *et al.*, *Phys. Rev. B* **81**, 195203 (2010).
 - [55] Y. Xia *et al.*, e-print arXiv:0812.2078 (2008).
 - [56] M. Hoesch, PhD dissertation, University of Zürich, (2002).
 - [57] S. Bengió *et al.*, *Surface Science* **601**, 2908 (2007).
 - [58] P. D. Johnson. *Rep. Prog. Phys.* **60**, 1217 (1997).
 - [59] Y. Kopelevich *et al.*, *Phys. Rev. B* **73**, 165128 (2006).
 - [60] A. Bostwick, T. Ohta, T. Seyller, K. Horn & E. Rotenberg, *Nature Phys.* **3**, 36 (2007).
 - [61] G. Jezequel, J. Thomas & I. Pollini, *Phys. Rev. B* **56**, 6620 (1997).
 - [62] C. R. Ast & H. Hochst, *Phys. Rev. B* **70**, 245122 (2004).
 - [63] D. N. Sheng, Z. Y. Weng, L. Sheng & F. D. M. Haldane, *Phys. Rev. Lett.* **97**, 036808 (2006).
 - [64] L. Sheng, D. N. Sheng, C. S. Ting & F. D. M. Haldane, *Phys. Rev. Lett.* **95**, 136602 (2005).
 - [65] T. K. Kim *et al.*, *Phys. Rev. B* **72**, 085440 (2005).
 - [66] D. M. Brown & S. J. Silverman, *Phys. Rev.* **136**, A290 (1964).
 - [67] L. M. Falicov & P. J. Lin, *Phys. Rev.* **141**, 562 (1965).
 - [68] H. Höchst & C. R. Ast, *J. Electron Spectrosc. Relat. Phenom.* **137**, 441 (2004).
 - [69] X. Gonze *et al.*, *Phys. Rev. B* **44**, 11023 (1991).

- [70] E. Kneedler, K. E. Smith, D. Skelton & S. D. Kevan,
Phys. Rev. **B44**, 8233 (1991).